AUDITOR – GA 687367

Advanced Multi-Constellation EGNSS Augmentation and Monitoring Network and its Application in Precision Agriculture

D6.3 Version 1.0

AUDITOR System Integration and Validation

Contractual Date of Delivery: 07/03/2018

Actual Date of Delivery: 07/03/2018

Editor: Alberto García-Rigo, Manuel Hernández-Pajares, David Roma-Dollase (UPC) Jacobo Domínguez, Esther López, David Abia (ACORDE), Carles Fernández-Prades, Marc Majoral, Javier Arribas (CTTC)

Author(s): Manuel Hernández-Pajares, Alberto García-Rigo, David Roma-Dollase (UPC) Jacobo Domínguez, Esther López, David Abia (ACORDE), Carles Fernández-Prades, Marc Majoral, Javier Arribas (CTTC)

Work package: WP6 - Integration and validation.

Security: Public

Nature: Report

Version: 1.0

Total number of pages: 93

Abstract:

This report is focused on the integration and validation process of the AUDITOR front-end, the software receiver as well as the Central Processing Facility of AUDITOR precise positioning corrections. In addition, results of likely the main elements of the full AUDITOR correction system (working in RT conditions, both the Central Processing Facility at the SE Europe, around Greece, and two permanent receivers treated as roving users, with induced cold starts each 3 hours. The measurements, preprocessed in RT, are reprocessed with the same software to assess the impact of the WARTK technique and characterizing in detail the CPF functioning and user performance, confirming the advantages of the technique.

Document Control

Version	Details of Change	Author	Approved	Date
1.0	Public version	All		2018-03-07

Executive Summary

This report is focused on the integration and validation of the AUDITOR front-end - software receiver as well as the Central Processing Facility of AUDITOR precise positioning corrections. In addition, and results of likely the main elements of the full AUDITOR correction system (which is working in RT conditions), both the Central Processing Facility at the SE Europe, around Greece, and two permanent receivers treated as roving users, with induced cold starts each 3 hours. The measurements, preprocessed in RT, are reprocessed with the same software to assess the impact of the WARTK technique and characterizing in detail the CPF functioning and user performance, confirming the advantages of the technique. Moreover, future updates of the system are envisaged, by implementing some of mitigation techniques on Medium Scale Travelling Ionospheric Disturbances developed by the UPC-IonSAT authors.

Authors

Partner	Name	e-mail
UPC	Manuel Hernández-Pajares	manuel.hernandez@upc.edu
	Alberto García Rigo	alberto.garcia.rigo@upc.edu
	David Roma Dollase	droma@el.ub.edu
ACORDE	Jacobo Domínguez	jacobo.dominguez@acorde.com
	Esther López	esther.lopez@acorde.com
	David Abia	david.abia@acorde.com
CTTC	Carles Fernández-Prades	carles.fernandez@cttc.es
	Marc Majoral	marc.majoral@cttc.es
	Javier Arribas	javier.arribas@cttc.es

Table of Contents

List of tables

List of figures

List of Acronyms and Abbreviations

Term	Description
BNC	BKG Ntrip Client
BS	B-spline
CPF	Central Processing Facility
dSTEC	Differential STEC
FE	Front-End
GIM	Global Ionospheric Maps
GNSS	Global Navigation Satellite System
GUI	Graphical User Interface
KPI	Key Performance Indicator
MSTID	Medium Scale TID
NABS	Non-uniform Adaptive B-splines
NTRIP	Network Transport RTCM via Internet Protocol
PVT	Position-Velocity-Time
RMS	Root Mean Square
RT	Real Time
RTK	Real Time Kinematic
SH	Spherical Harmonic
SSR	RTCM’s State Space Representation
STEC	Slant TEC
SW	Software
TEC	Total Electron Content
TID	Travelling Ionospheric Disturbance
TOMION	TOmographic Model of the IONosphere
UPC	Universitat Politècnica de Catalunya
VTEC	Vertical TEC
WARTK	Wide Area RTK
ZTD	Zenith Tropospheric Delays

1 AUDITOR GNSS-SDR validation

1.1 General Overview

1.1.1 Overall architecture from D6.1

Figure 1.1 depicts the architecture of the RF Front-End (FE) and the full GNSS-SDR receiver.

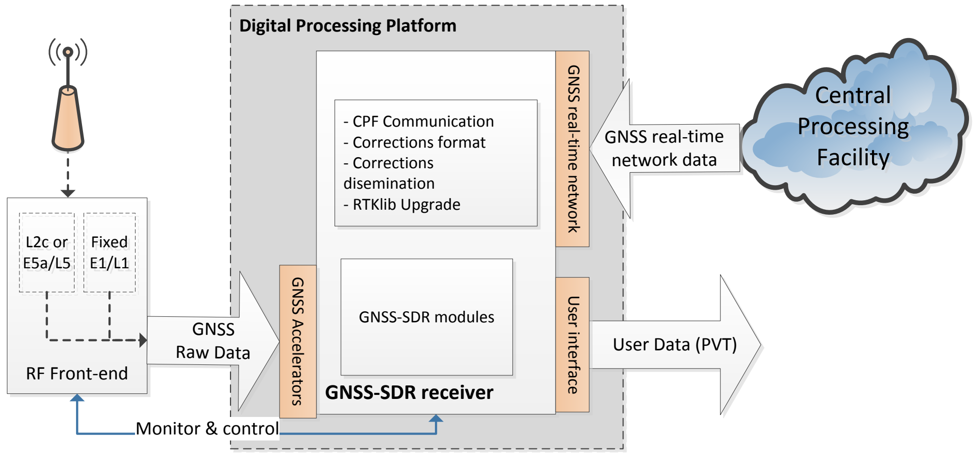

Figure 1.1 :GNSS-SDR receiver

The workflow of signal is:

- The **GNSS-SDR receiver** acquires the GNSS Raw data (L1, L2c or L5) **through the FE**.
- The GNSS-SDR receiver sends its observables to the **CPF** in order to apply real-time iBOGART corrections at the CPF and perform the PVT.
- The final PVT information needs to be calculated at the CPF and provided to the end user.

Two versions of the FE have been designed, manufactured and tested v1.0 and v2.0. Taking into account the software-defined radio implementation of the presented GNSS receiver, the validation of the FE is tightly coupled to the GNSS-SDR baseband processing.

Early validation of the FE v2.0, while the GNSS-SDR real-time accelerators for the proposed bands (E1/L1, L2C, E5a/L5) were being implemented and tested, was possible thanks to initial Linux implementation of the GNSS-SDR software that could process FE measurements in an offline model with a standard computer.

2 AUDITOR corrections validation

2.1 TOMION working in real-time at the Central Processing Facility side

The real-time implementation of the AUDITOR Central Processing Facility (CPF) has been set up during December 2017. Since then it has been running in different short sessions, and now continuously (after doubling the hard disk capacity of our server chapman.upc.es). The purpose is to characterize the performance in realistic conditions, without depending on the availability of the final AUDITOR hardware and user software versions. In this way we will be able to identify in advance potential improvements for future upgrades of the main elements of TOMION implementing the WARTK technique in the AUDITOR scenario. We are focusing here on a detailed analysis of the first session, run around the Christmas (since afternoon of 24th December to noon of 26th December, days 357 to 359 of year 2017). We have summarized the results obtained at 1 Hz, showing the equivalent ones at 30 seconds rate.

2.1.1 Real-time WARTK network, users and dates

After studying the stability and latency of the GPS measurements provided by available RTCM GNSS streams, the network of permanent receiver has been selected for supporting AUDITOR in Greece, its target region. It consists of 6 permanent receivers supporting the WARTK CPF: MATE, ORID, KTCH, DYNG, ISTA, and SOFI as the reference receiver for satellite clock estimation and carrier phase double differencing. Moreover the observations of two additional permanent receivers, AUT1 and PVOG, are being ingested as “rover-like” receivers (see Figure 2.1), i.e. without significant weight in the CPF, modelling as kinematic user and with its different, WARTK user ambiguity fixing algorithm (see in particular Hernández-Pajares et al. 2000 [3]). This is a simple way of taking and assessing in real-time the fresh WARTK corrections, in particular differential corrections in the original format modelled by the CPF: satellite clock estimation and ionospheric two-layer grid model corrections. The observations are taken at 1 Hz with a maximum tolerance of 2 seconds of latency (see its distributions in form of number of phase arc for the reference and rover-like receivers, SOFI and AUT1, in Figure 2.2).

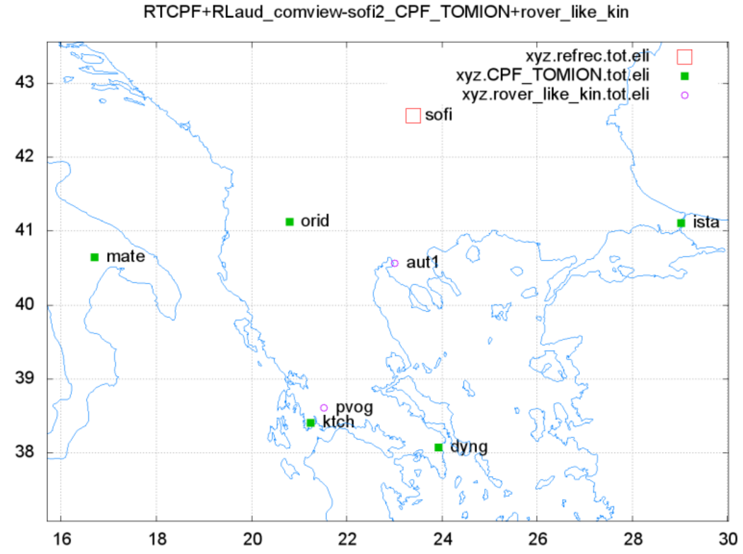

Figure 2.1 Map of the AUDITOR RT permanent GPS stations (green squares), including the reference one (red square) and permanent GPS receivers treated as rover users (magenta circles).

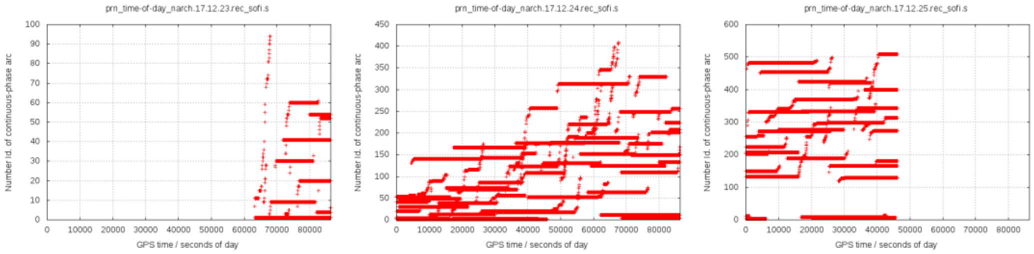

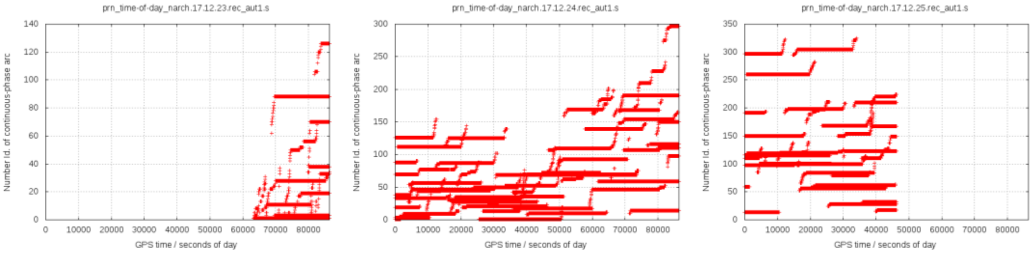

Figure 2.2 Number of continuous arc transmitter-receiver vs time, for the reference GPS receiver SOFI (first row) and for one of the roving users, AUT1 (second row), during the first (starting-up), second and third, and last, days of this RT experiment (days 23, 24 and 25 December 2017, respectively).

2.1.2 Triple differences of prefit residuals

Both the real-time cycle-slip detection (based on the discontinuities of the ionospheric carrier phase and phase-pseudorange Melbourne-Wubbena combinations see for instance Blewitt 1990, [1]) and the modelling of the different observations (first-order-free ionospheric and ionospheric combinations of carrier phase and pseudoranges, Lc, Pc, Li and Pi respectively, and Melbourne-Wubbena combination) can be independently checked by means of the triple differences of Lc (once the receiver positioning is known in advance at cm-error level) regarding to the reference satellite (with highest elevation), reference receiver (SOFI) and consecutive observation times (1 Hz in actual conditions, or 30 seconds in this detailed assessment). Figure 2.3 and Figure 2.4 show that the algorithm works well (just few low elevation observations show undetected cycle-slips).

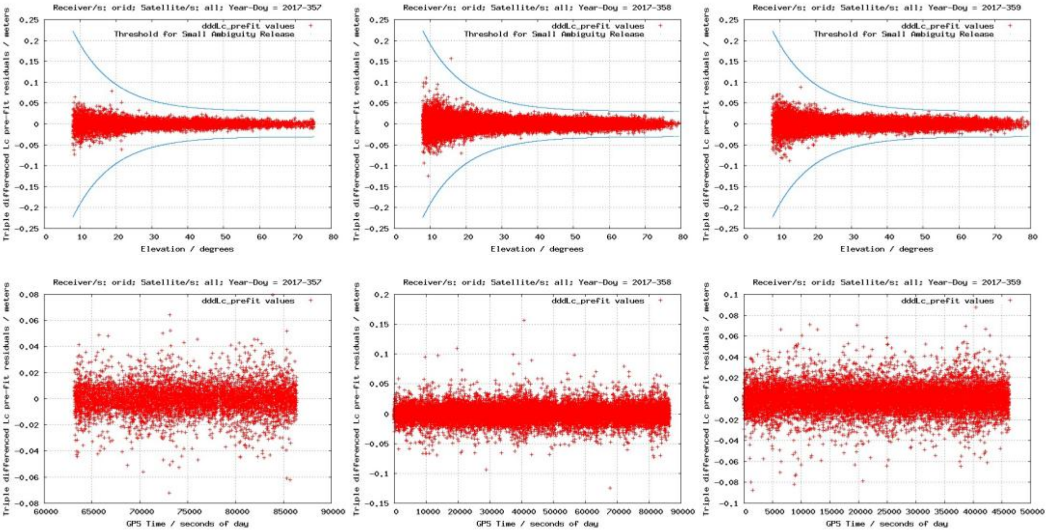

Figure 2.3 Triple differences of ionospheric-free combination of carrier phases for the permanent receiver ORID, vs elevation (first row) and vs time (second row), during the first (starting-up), second and third, and last, days of this RT experiment (days 23, 24 and 25 December 2017, respectively).

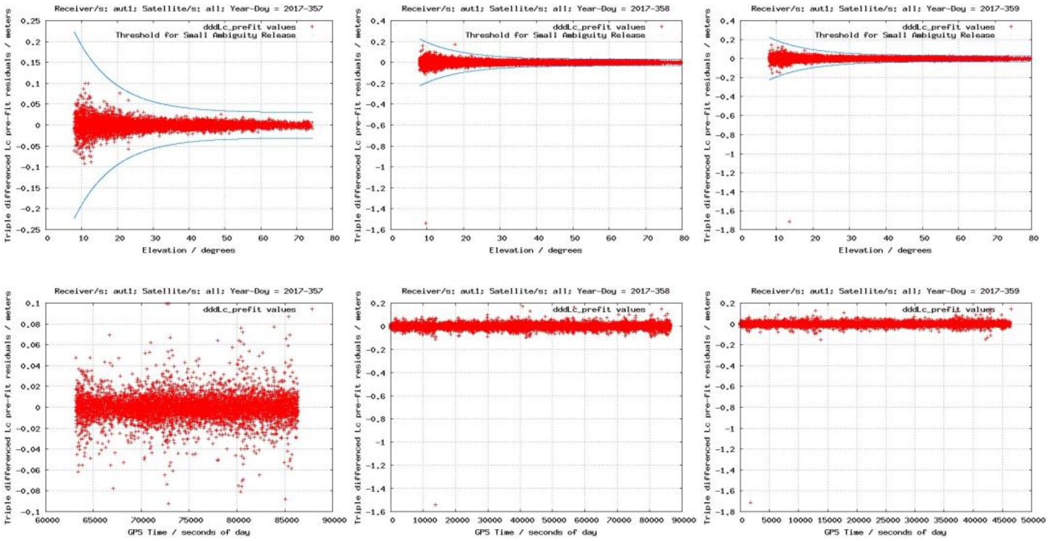

Figure 2.4 Triple differences of ionospheric-free combination of carrier phases for the roving user AUT1, versus elevation (first row) and versus time (second row), during the first (starting-up), second and third, and last, days of this RT experiment (days 23, 24 and 25 December 2017, respectively).

2.1.3 RT GPS satellite clocks estimated by the AUDITOR CPF vs the IGS ones

The implementation of the differential processing is performed by TOMION by means of an undifferenced model, but sharing the receiver clock errors, referred to the permanent receiver clock error, as far as its carrier phase ambiguities, with the users. Then the checking of the satellite clocks estimated by the WARTK CPF is convenient to see the correct functioning of the CPF in spite of this not a target by itself (they should be properly computed from a global GNSS network, not from a regional one). In next figures the real-time satellite clock estimates from AUDITOR WARTK network is compared with the final values estimated globally by the IGS analysis centers. It can be seen in general the remarkable consistency of the results (see Figure 2.5, Figure 2.6, Figure 2.7, Figure 2.8, Figure 2.9 and Figure 2.10).

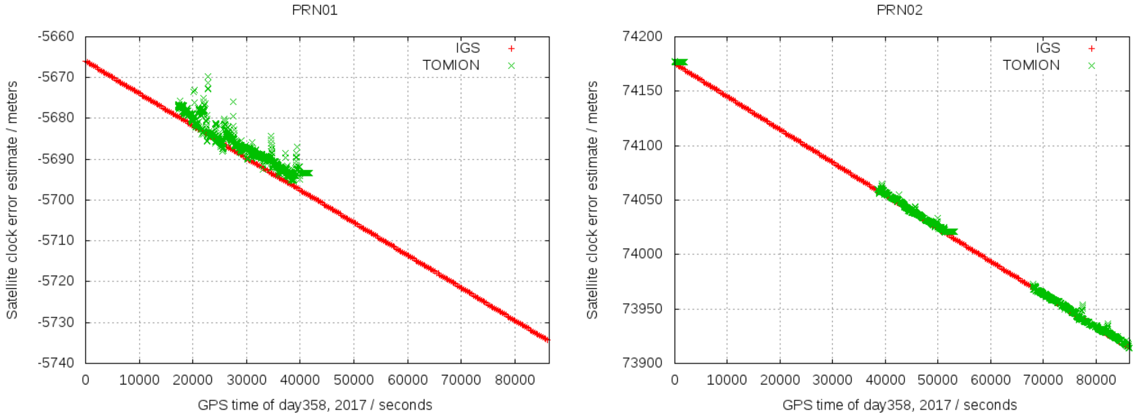

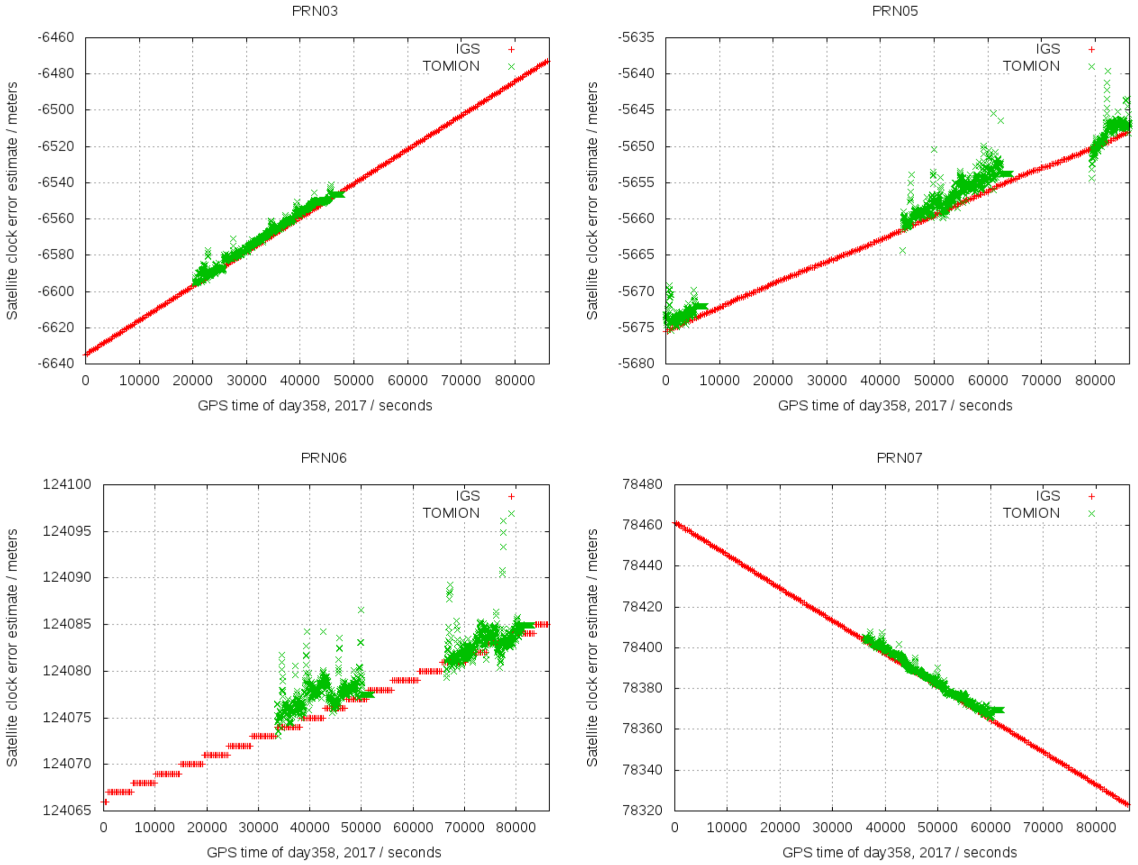

Figure 2.5 Satellite clock offsets for GPS satellites (PRN01, 02, 03, 05, 06 and 07 from left to right and from top to bottom) estimated by the CPF for the different satellites in view (green points) versus the final values computed and combined in post-processed by IGS analysis centers. during the second day of this RT experiment (day 24 December 2017).

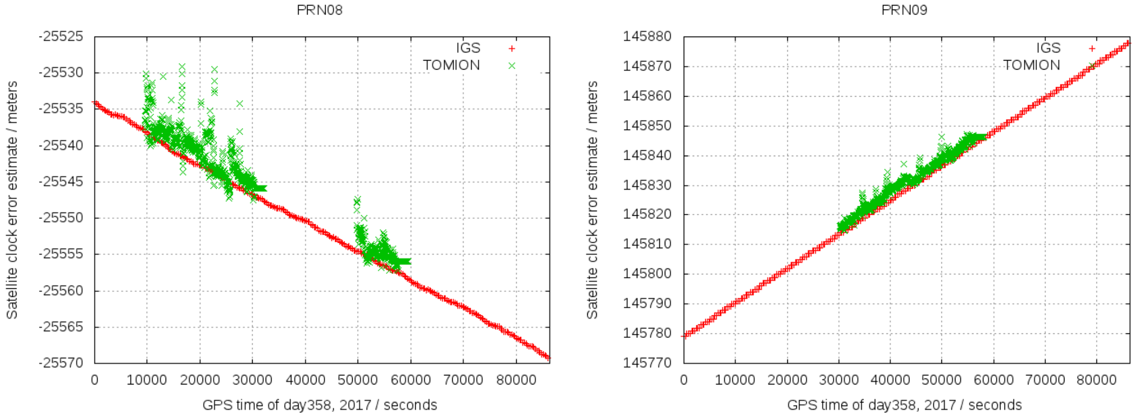

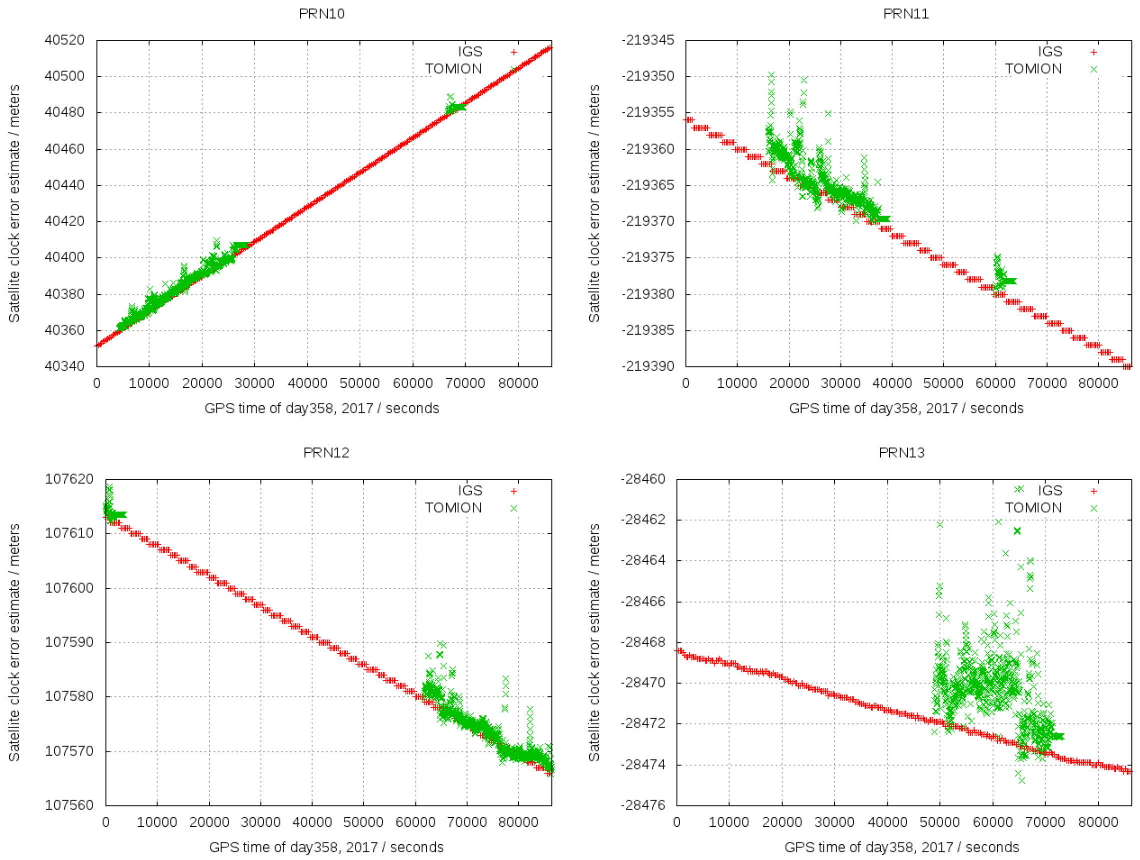

Figure 2.6 Satellite clock offsets for GPS satellites (PRN08, 09, 10, 11, 12 and 13 from left to right and from top to bottom) estimated by the CPF for the different satellites in view (green points) versus the final values computed and combined in post-processed by IGS analysis centers. during the second day of this RT experiment (day 24 December 2017).

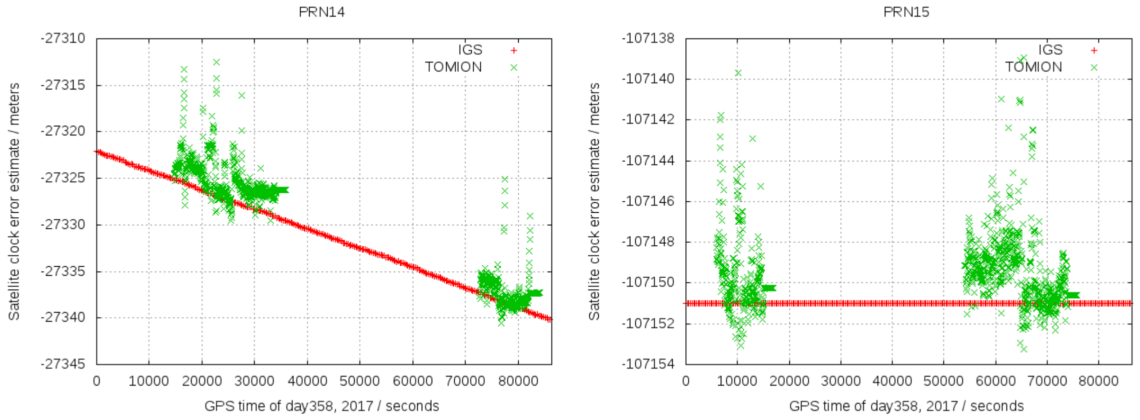

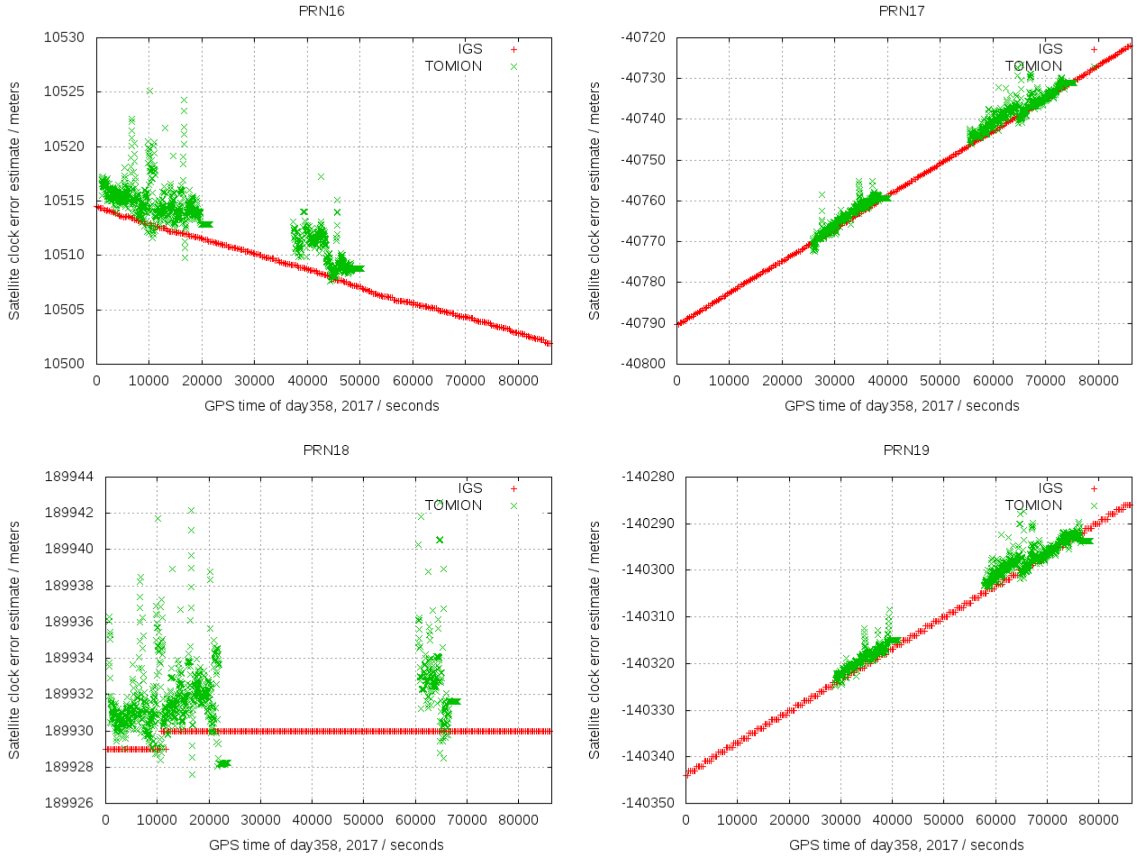

Figure 2.7 Satellite clock offsets for GPS satellites (PRN14, 15, 16, 17, 18 and 19 from left to right and from top to bottom) estimated by the CPF for the different satellites in view (green points) versus the final values computed and combined in post-processed by IGS analysis centers. during the second day of this RT experiment (day 24 December 2017).

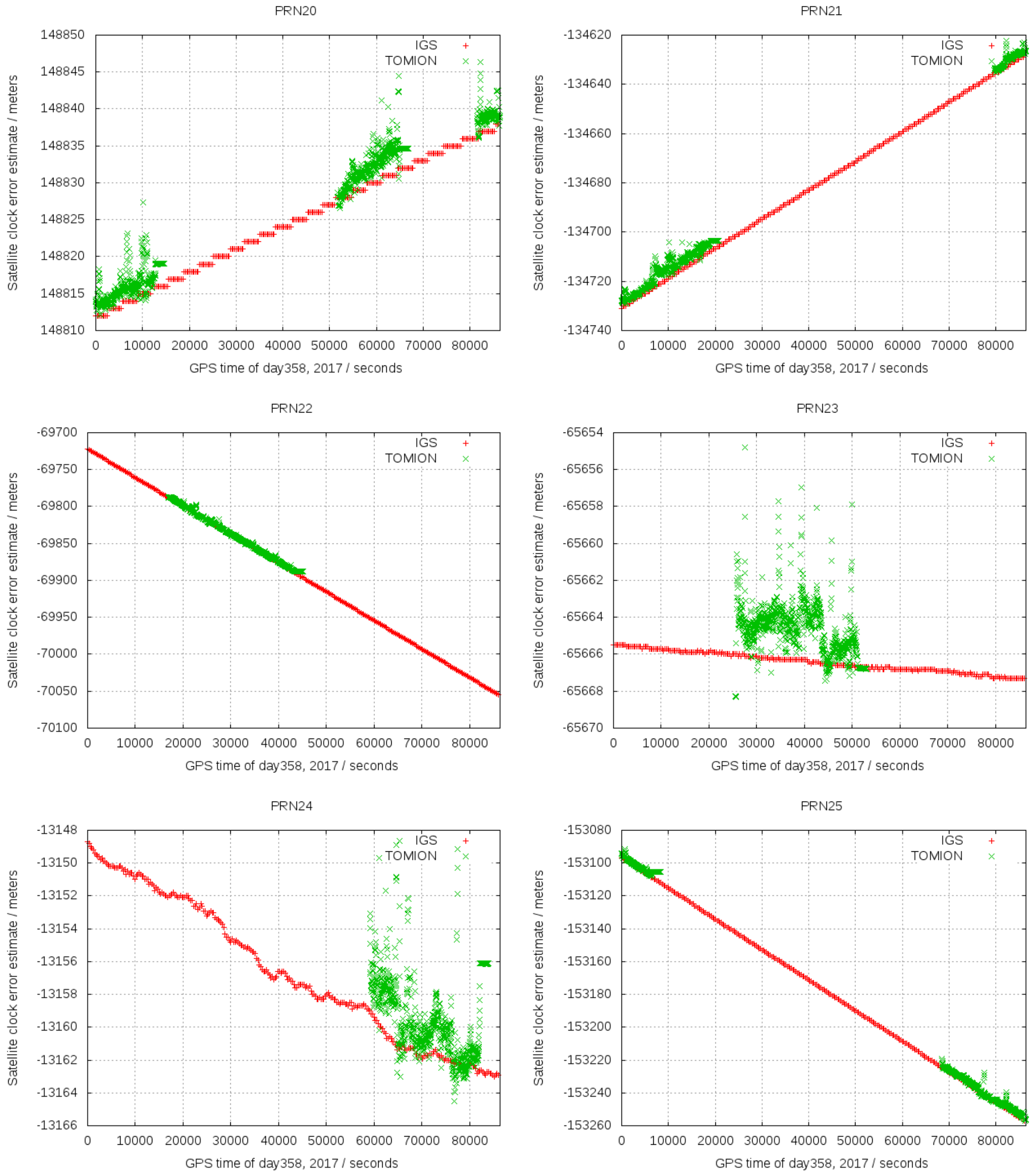

Figure 2.8 Satellite clock offsets for GPS satellites (PRN20, 21, 22, 23, 24 and 25 from left to right and from top to bottom) estimated by the CPF for the different satellites in view (green points) versus the final values computed and combined in post-processed by IGS analysis centers. during the second day of this RT experiment (day 24 December 2017).

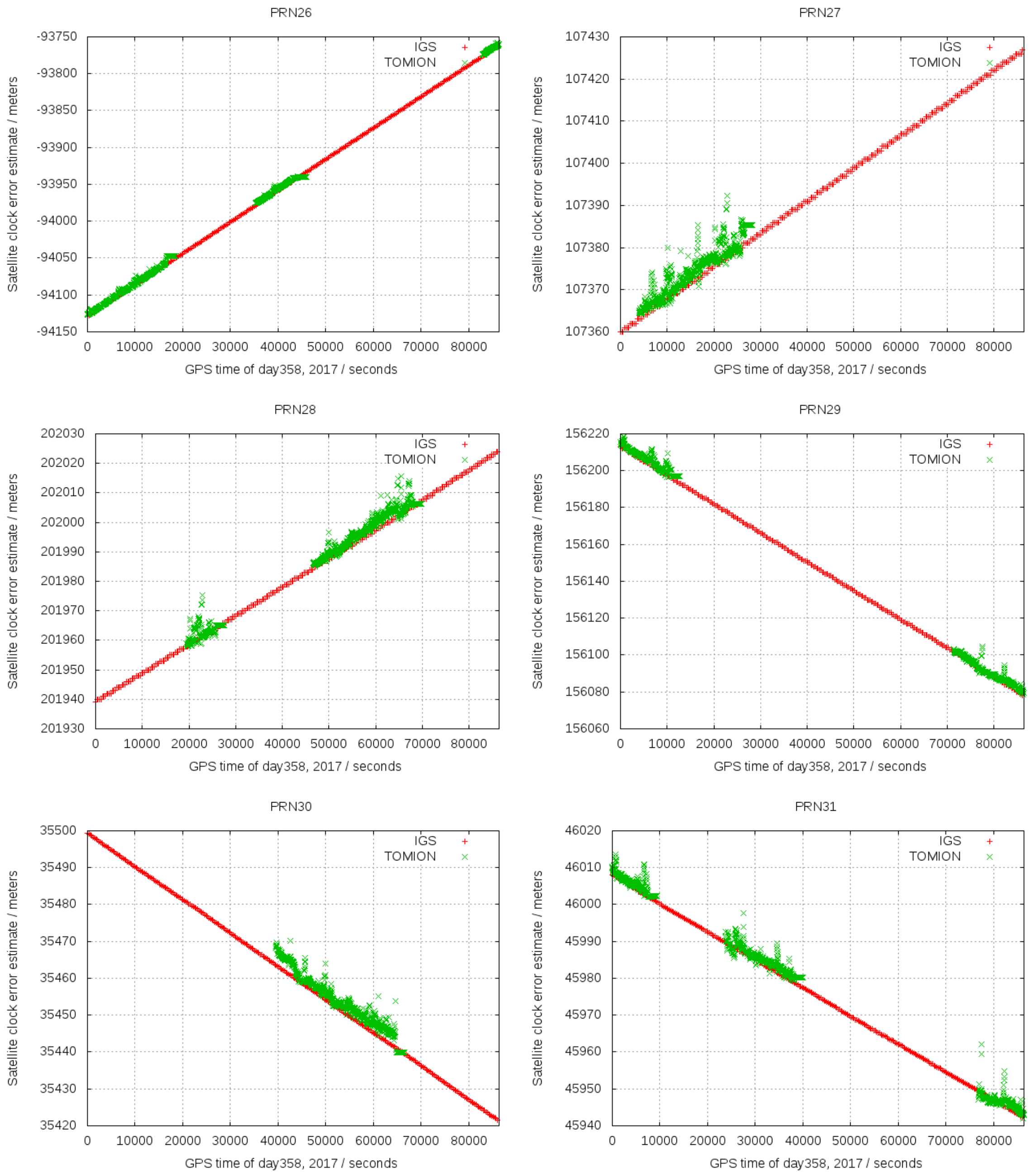

Figure 2.9 Satellite clock offsets for GPS satellites (PRN26, 27, 28, 29, 30 and 31 from left to right and from top to bottom) estimated by the CPF for the different satellites in view (green points) versus the final values computed and combined in post-processed by IGS analysis centers. during the second day of this RT experiment (day 24 December 2017).

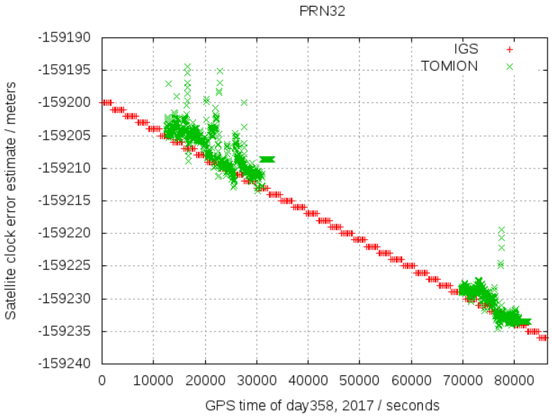

Figure 2.10 Satellite clock offsets for GPS satellites (PRN32 from left to right and from top to bottom) estimated by the CPF for the different satellites in view (green points) versus the final values computed and combined in post-processed by IGS analysis centers. during the second day of this RT experiment (day 24 December 2017).

2.1.4 RT Zenith Tropospheric Delay estimated by the AUDITOR CPF vs the IGS ones

Another real-time product very sensitive to the quality of the CPF processing is the Zenith Tropospheric Delay, estimated as random walk in the CPF filter. It can be seen a noisier but mostly unbiased behavior, when compared with the post-processed global combined solution of IGS (see Figure 2.11) in spite of the limitations in the relative positioning for ZTD determination. On the other hand it can be seen (Figure 2.12) the very challenging ZTD estimation by the two users, where the effect of the warm start of the roving user filter (all the unknowns treated as white noise each 3 hours) is evident, and a first guess of the convergence time can be seen in terms of ZTD.

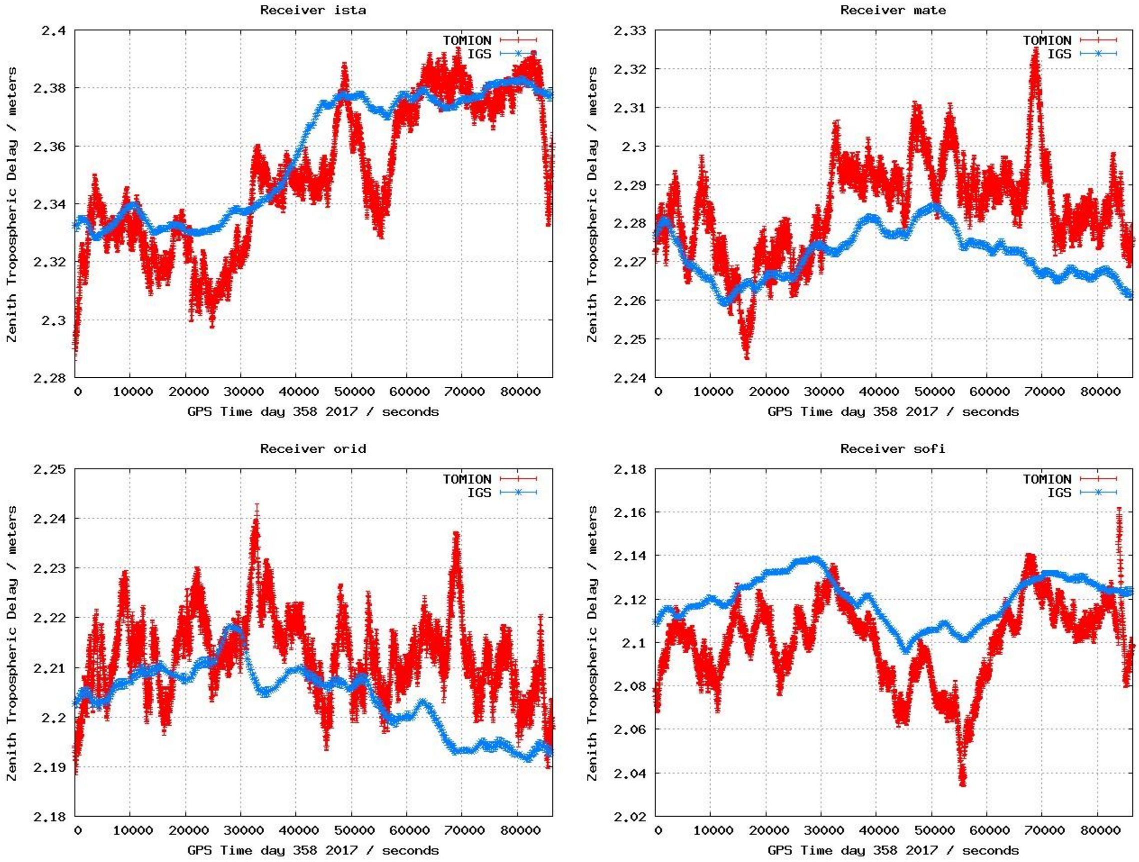

Figure 2.11 Zenith Tropospheric Delay estimated in RT by the AUDITOR CPF (red) for permanent receivers with available final IGS estimation (blue), from left to right and from top to bottom the receivers ISTA, MATE, ORID and SOFI, during the second day of this RT experiment (24 December 2017).

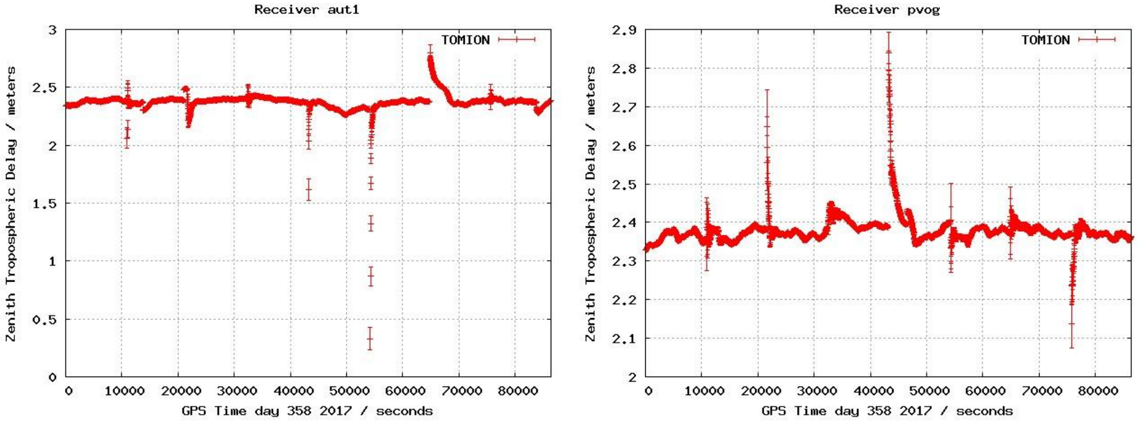

Figure 2.12 Zenith Tropospheric Delay estimated in RT by the WARTK users of AUDITOR, AUT1 (left) and PVOG (right), during the second day of this RT experiment (day 24 December 2017).

2.1.5 RT Vertical Total Electron Content (VTEC) estimated by the AUDITOR CPF vs the presently more accurate IGS GIM (UQRG)

WARTK is a hybrid model combining in a synergic way the “geometric”, non-frequency dependent, model and the ionospheric, frequency dependent, one. In order to assess the accuracy of the RT ionospheric determination, a comparison of the RT-VTEC, obtained from vertical summation within the tomographic grid, with the post-processed VTEC provided by one of the best, or the best presently VTEC GIMs in IGS (Roma-Dollase et al. 2017, [7]), is shown in Figure 2.13. This GIM is computed daily by UPC-IonSAT with Id. “UQRG”, combining tomography with kriging interpolation, and distributed from IGS servers. The RT STECs vs time and elevation for the overall receivers are shown in Figure 2.14 and Figure 2.15 respectively.

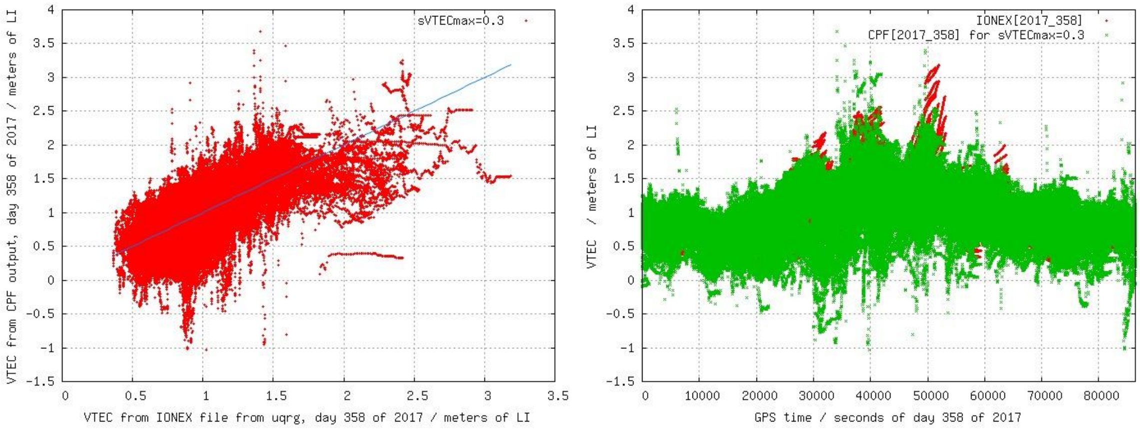

Figure 2.13 In the left-hand plot the VTEC estimated in RT by the CPF (vertical axis) vs the reference value provided by the post-processed Global Ionospheric Map (GIM) UQRG (horizontal axis, both in meters of LI=L1-L2) is represented, and the corresponding time evolution (in green and red, respectively) is shown at the right-hand plot, both during the second day of this RT experiment (day 24 December 2017).

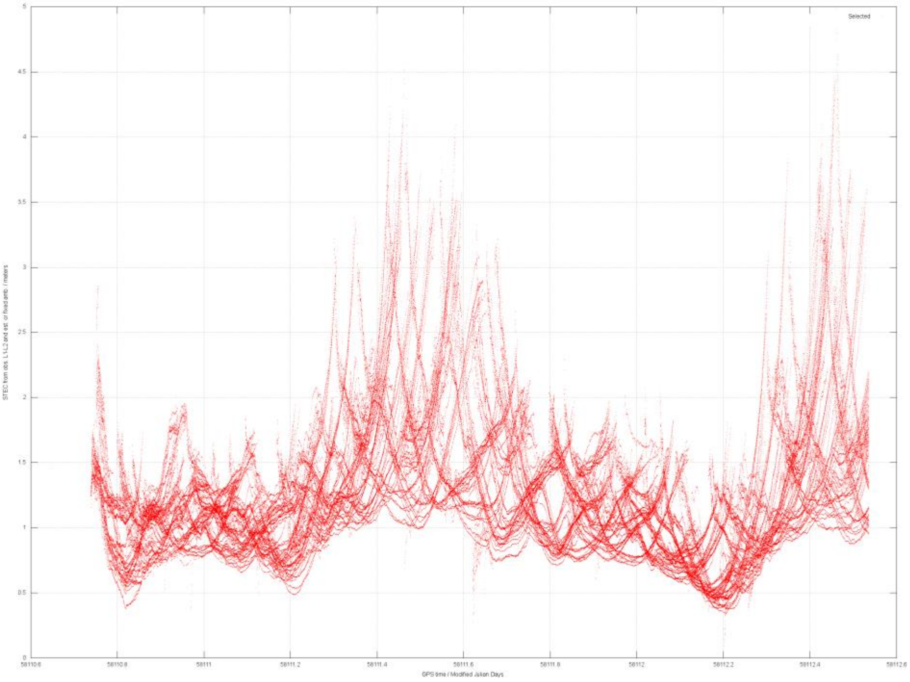

Figure 2.14 STEC estimated in RT by the CPF (vertical axis in meters of LI=L1-L2) vs time (horizontal axis in modified julian days) is represented, during the whole RT experiment (days 23, 24 and 25 December 2017).

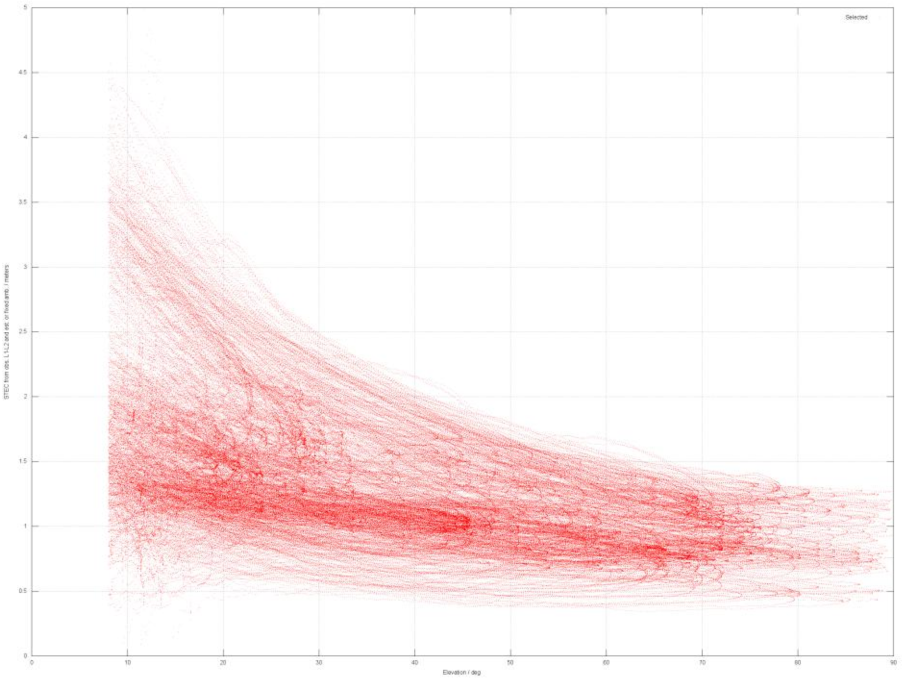

Figure 2.15 STEC estimated in RT by the CPF (vertical axis in meters of LI=L1-L2) vs elevation angle above the horizon (horizontal axis in degrees) is represented, during the whole RT experiment (days 23, 24 and 25 December 2017).

2.1.6 RT VTEC model fitted independently for each satellite in view from the RT WARTK AUDITOR estimation (broadcasted as message DSM)

The ionospheric corrections are broadcast to the users in terms of an independent linear fit of the VTEC per satellite, from the STECs determined in RT for the permanent receivers by the WARTK model (implemented in terms of the DSM message). The bias and RMS of such fitting, and the residuals themselves, are shown in Figure 2.16, Figure 2.17 and Figure 2.18 for the central day. They are reasonable, excepting from 45000 to 60000 seconds (see discussion below). The time evolution of the three coefficients per satellite are also shown in Figure 2.19, Figure 2.20, Figure 2.21, Figure 2.22, Figure 2.23 and Figure 2.24.

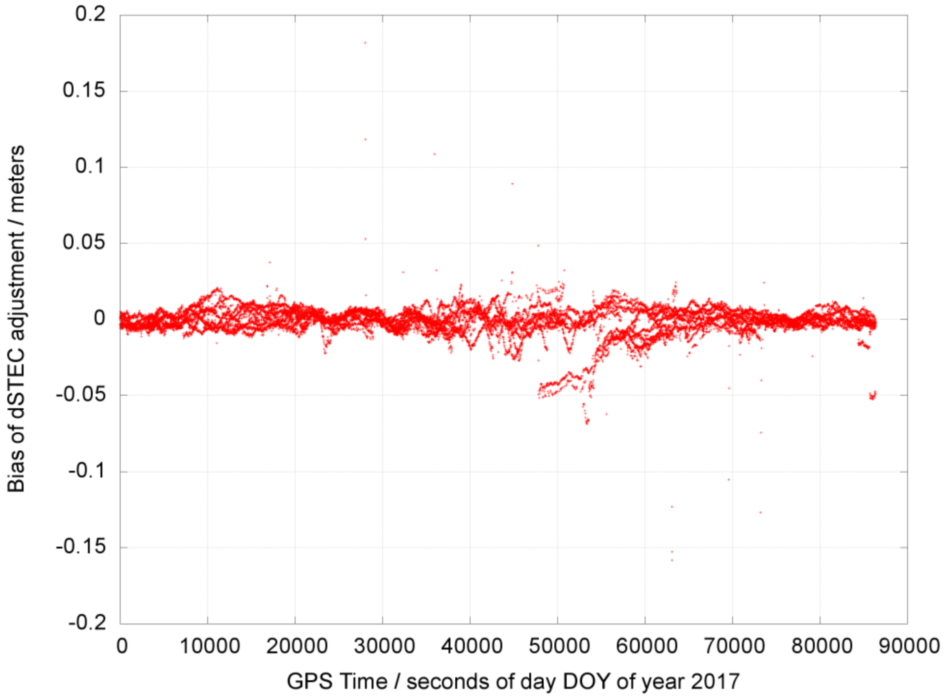

Figure 2.16 The bias of the residuals of the VTEC fitting per satellite (vertical axis in meters of LI=L1-L2) vs time (horizontal axis in seconds of the day) is represented, during the second day of the RT experiment (day 24 December 2017).

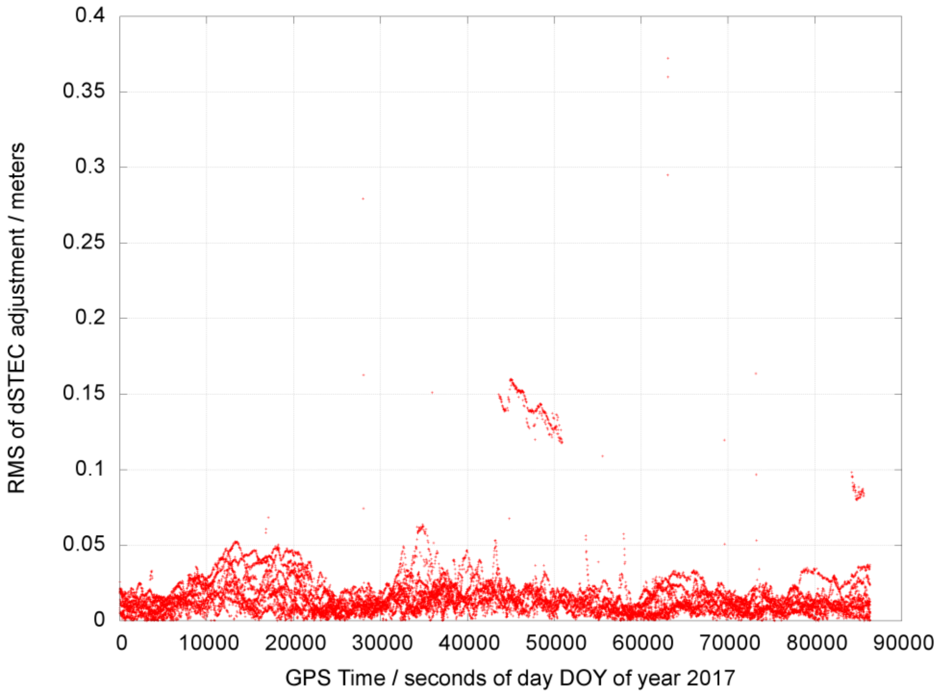

Figure 2.17 The RMS of the residuals of the VTEC fitting per satellite (vertical axis in meters of LI=L1-L2) vs time (horizontal axis in seconds of the day) is represented, during the second day of the RT experiment (day 24 December 2017).

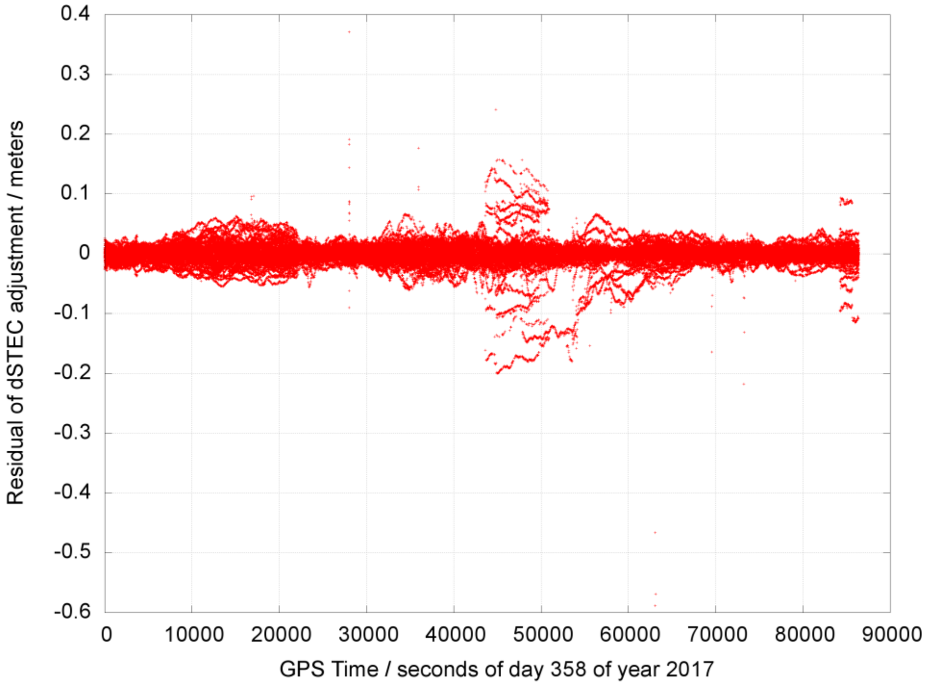

Figure 2.18 Residuals of the VTEC fitting per satellite (vertical axis in meters of LI=L1-L2) vs time (horizontal axis in seconds of the day) is represented, during the second day of the RT experiment (day 24 December 2017).

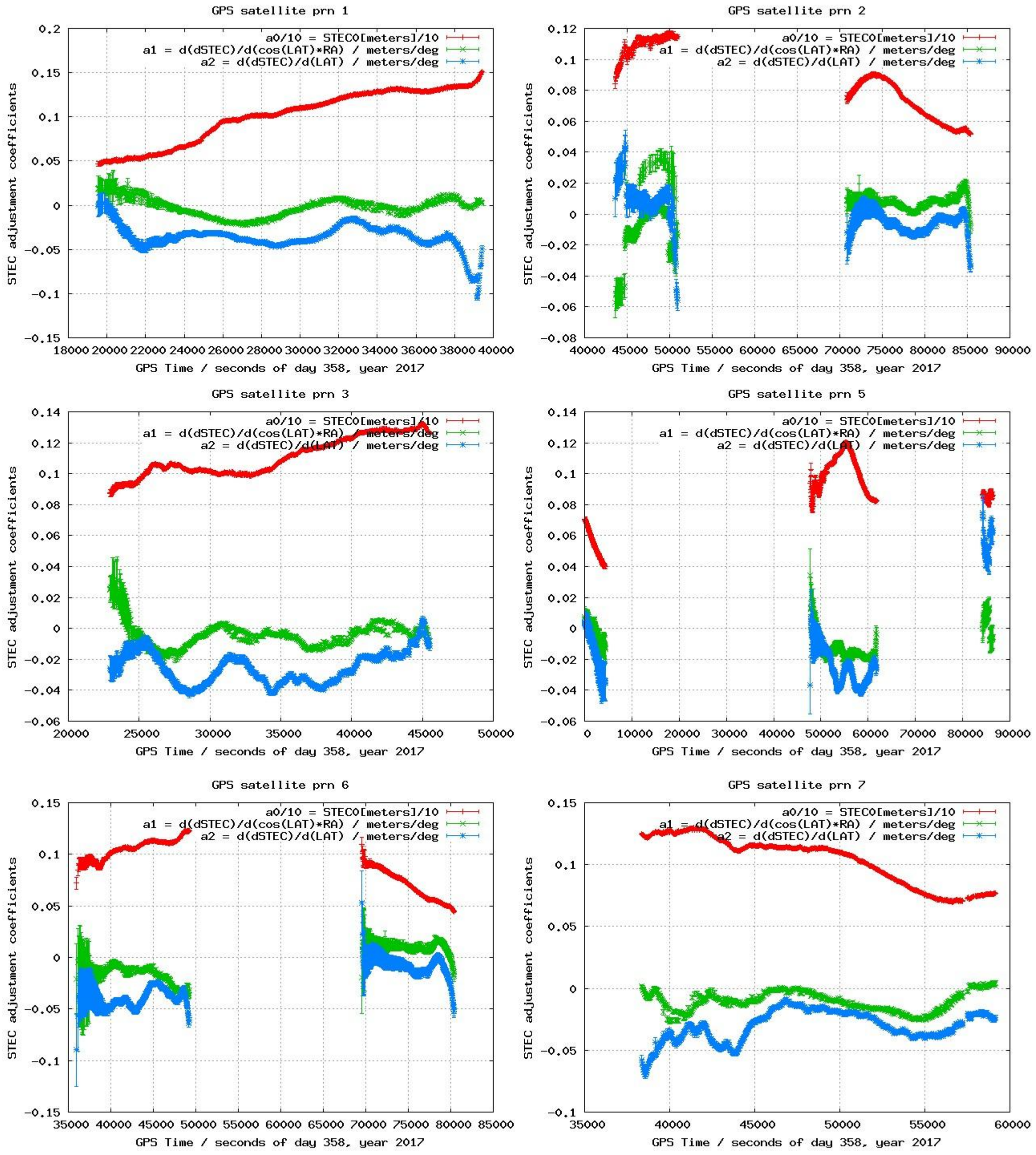

Figure 2.19 Coefficients of the VTEC fitting per satellite (vertical axis) vs time (horizontal axis in seconds of the day) is represented, from left to right and from top to bottom, for satellites PRN01, 02, 03, 05, 06 and 07, during the second day of the RT experiment (day 24 December 2017).

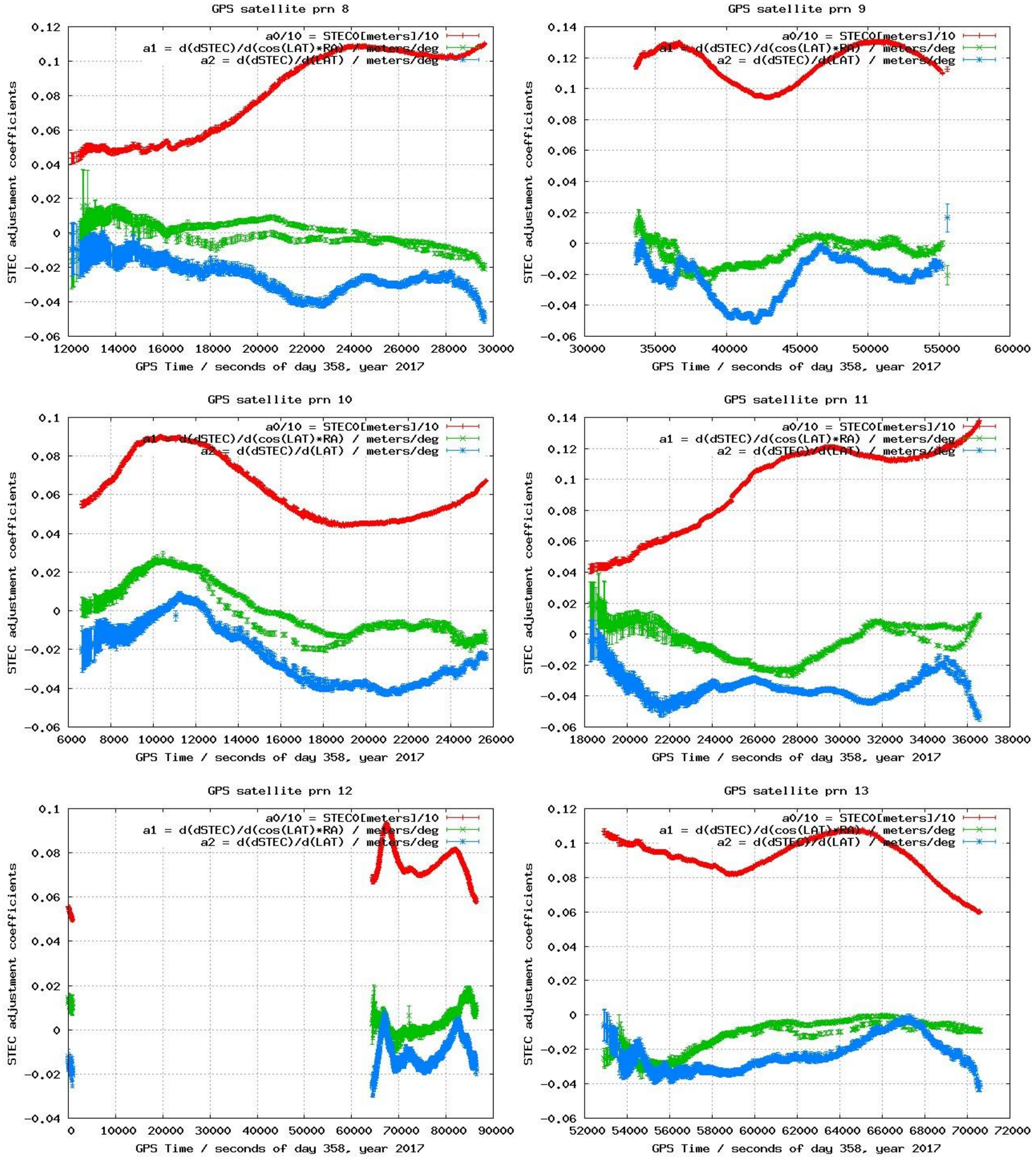

Figure 2.20 Coefficients of the VTEC fitting per satellite (vertical axis) vs time (horizontal axis in seconds of the day) is represented, from left to right and from top to bottom, for satellites PRN08, 09, 10, 11, 12 and 13, during the second day of the RT experiment (day 24 December 2017).

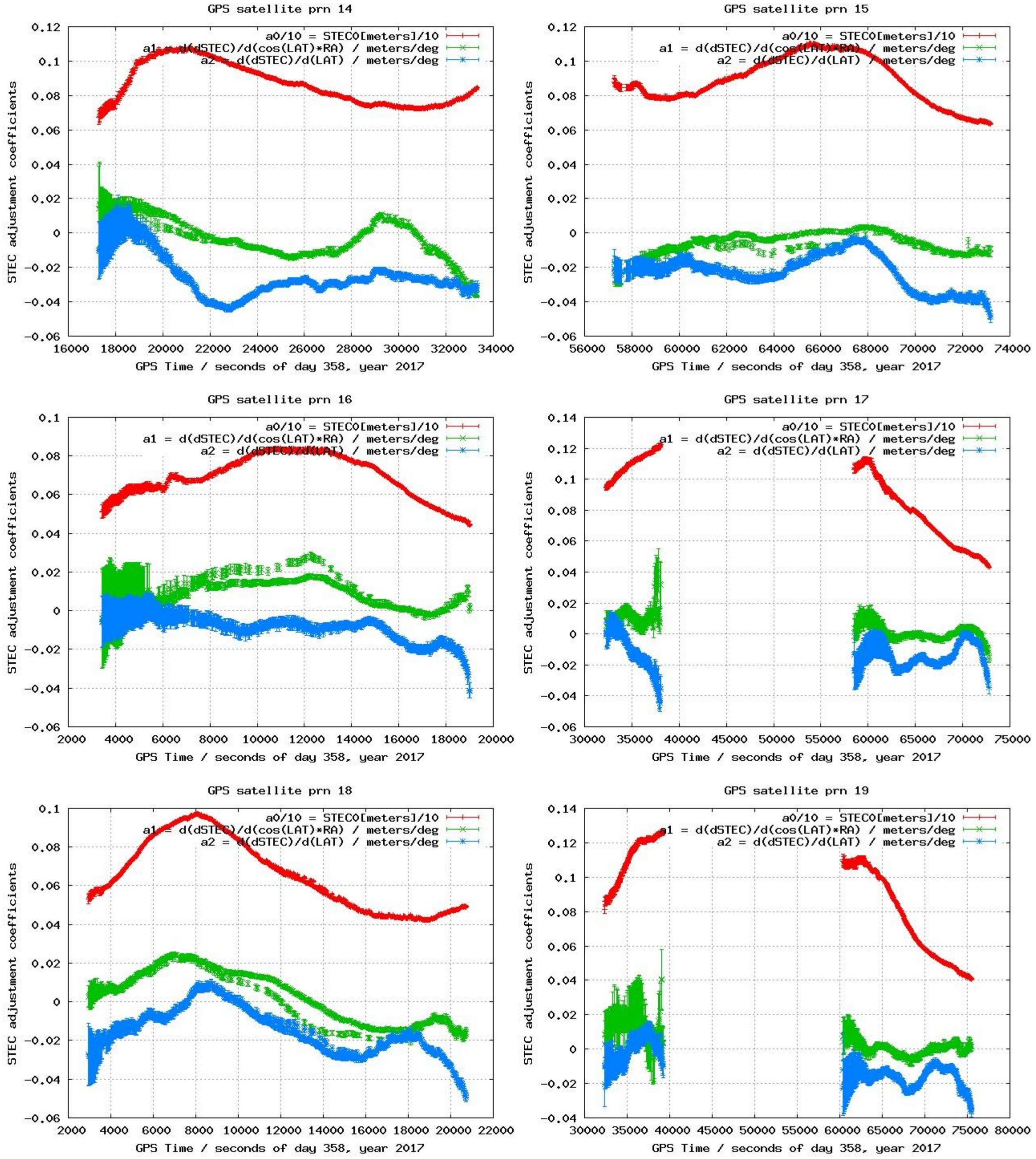

Figure 2.21 Coefficients of the VTEC fitting per satellite (vertical axis) vs time (horizontal axis in seconds of the day) is represented, from left to right and from top to bottom, for satellites PRN14, 15, 16, 17, 18 and 19, during the second day of the RT experiment (day 24 December 2017).

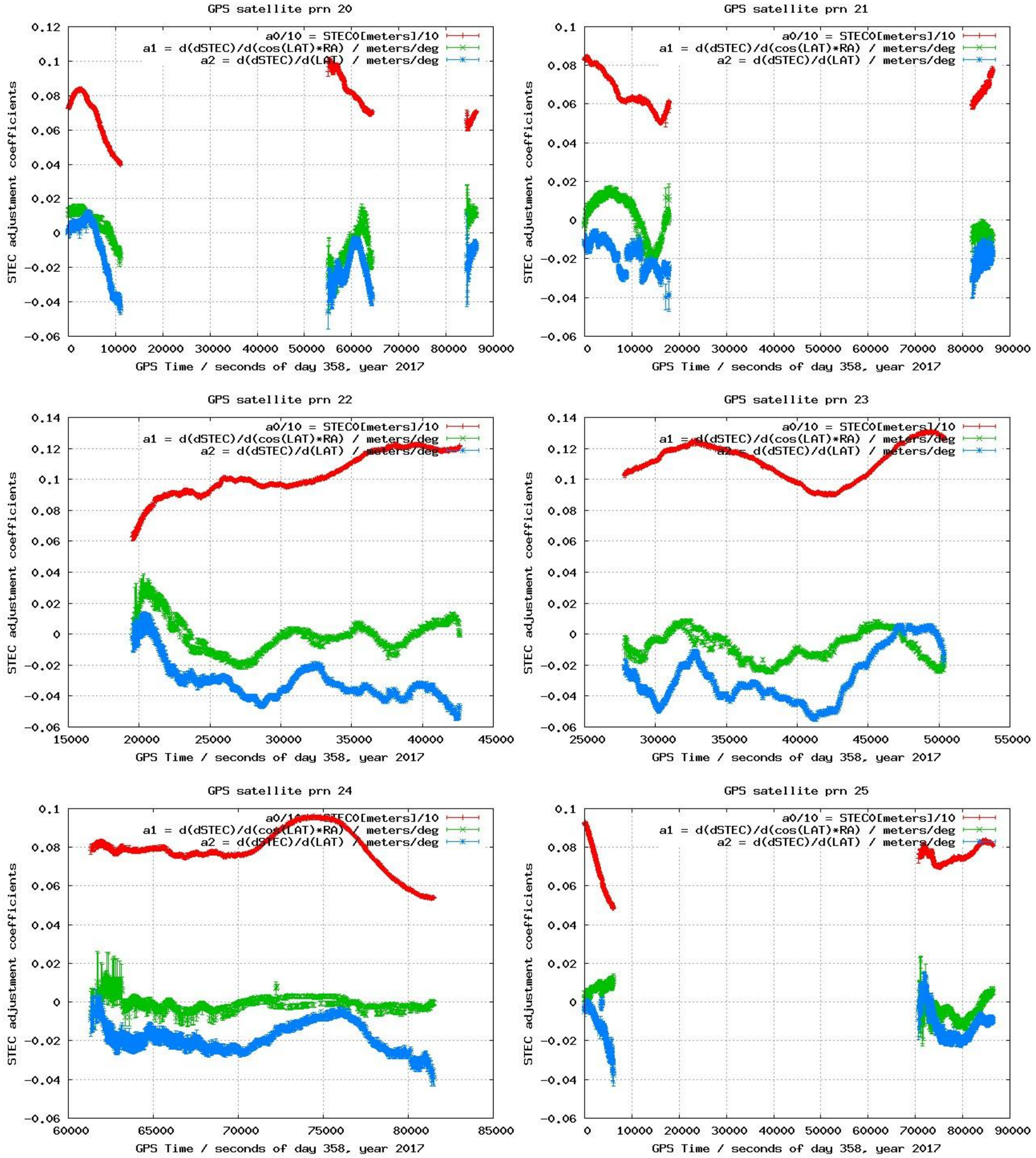

Figure 2.22 Coefficients of the VTEC fitting per satellite (vertical axis) vs time (horizontal axis in seconds of the day) is represented, from left to right and from top to bottom, for satellites PRN20, 21, 22, 23, 24 and 25, during the second day of the RT experiment (day 24 December 2017).

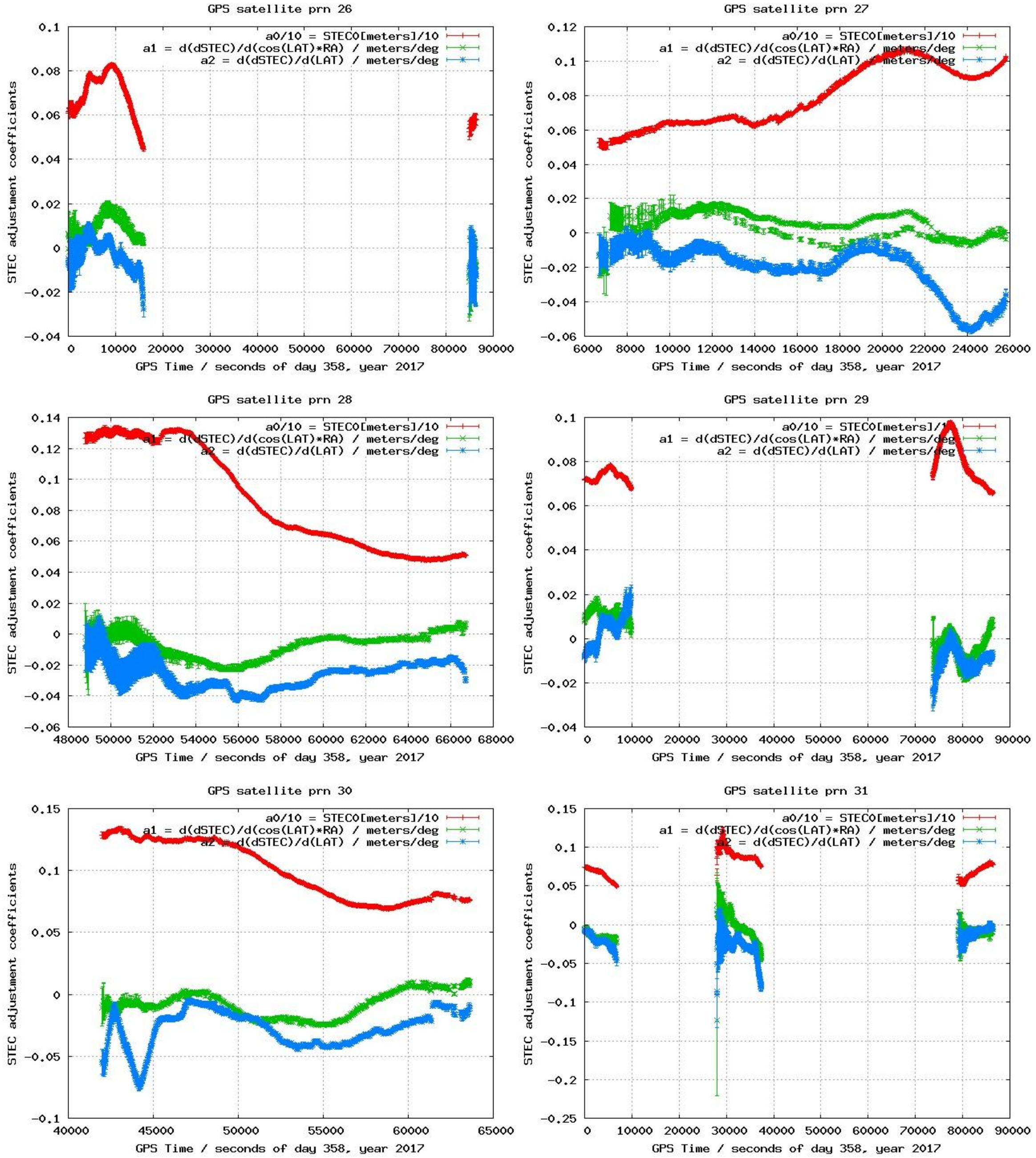

Figure 2.23 Coefficients of the VTEC fitting per satellite (vertical axis) vs time (horizontal axis in seconds of the day) is represented, from left to right and from top to bottom, for satellites PRN26, 27, 28, 29, 30 and 31, during the second day of the RT experiment (day 24 December 2017).

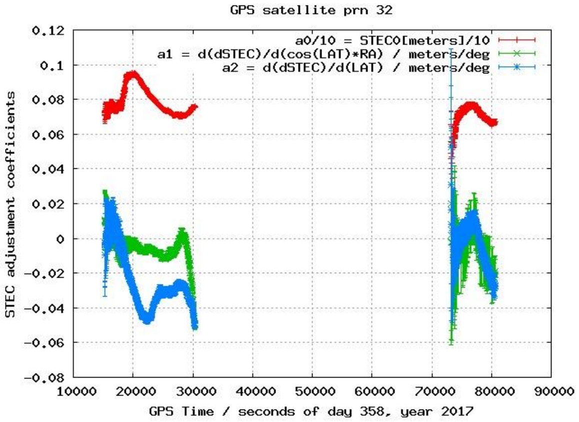

Figure 2.24 Coefficients of the VTEC fitting per satellite (vertical axis) vs time (horizontal axis in seconds of the day) is represented, from left to right and from top to bottom, for satellite PRN32, during the second day of the RT experiment (day 24 December 2017).

2.1.7 RT double-differenced carrier phase ambiguity fixing for the roving user AUT1 and for one typical permanent receiver (ORID)

A summary of the carrier phase ambiguity fixing is provided in this section. In Figure 2.25, the selected reference satellite (the one with highest elevation in the RT implementation) is represented versus time. In Figure 2.26 the double differenced ambiguity determined from the ionospheric-free and ionospheric ambiguities Bc and Bi is represented vs the values directly obtained from the Melbourne-Wübbena combination, for the roving user AUT1 and the permanent receiver ORID. It can be seen a good agreement, especially for the permanent receiver, as expected. The corresponding differences are represented versus elevation in Figure 2.27 and versus time in Figure 2.28. The widelane ambiguity fixing is reached sometimes up to 100%, and the second ambiguity to be fixed (see for instance Hernandez-Pajares et al. 2000), the narrowlane, is fixed up to 60% approximately (Figure 2.29).

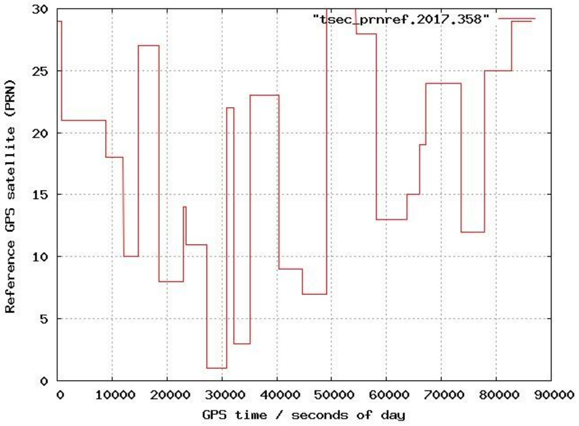

Figure 2.25 PRN of the GPS reference satellite selected in RT to form the double differences (the one available with maximum elevation seen from the reference receiver SOFI) versus time during the second day of the RT experiment (day 24 December 2017).

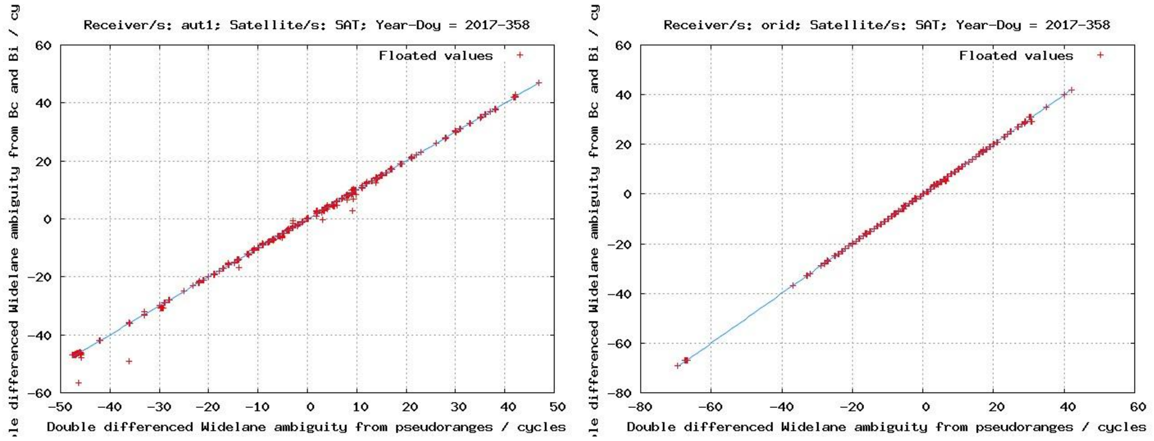

Figure 2.26 Double differenced widelane ambiguity, derived from the ionospheric-free and geometric-free double-differenced ambiguities, versus the value provided by the double-differenced ionospheric and geometric-free Melbourne-Wübbena combination, in cycles: left-hand plot correspond to the roving receiver AUT1 and the right-hand plot to the permanent receiver ORID, both during the second day of the RT experiment (day 24 December 2017).

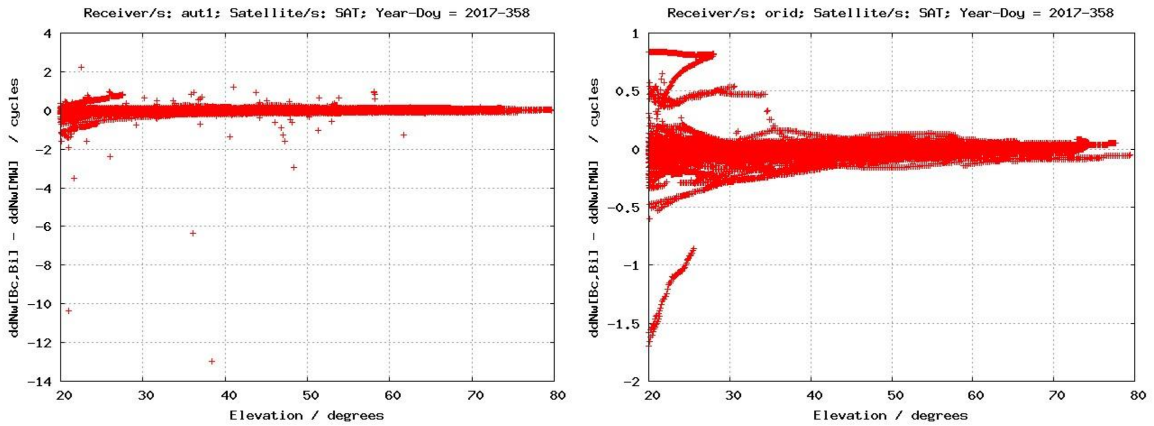

Figure 2.27 Difference of the double differenced widelane ambiguity, derived from the ionospheric-free and geometric-free double-differenced ambiguities, minus the value provided by the double-differenced ionospheric and geometric-free Melbourne-Wübbena combination, in cycles, versus elevation angle: left-hand plot correspond to the roving receiver AUT1 and the right-hand plot to the permanent receiver ORID, both during the second day of the RT experiment (day 24 December 2017).

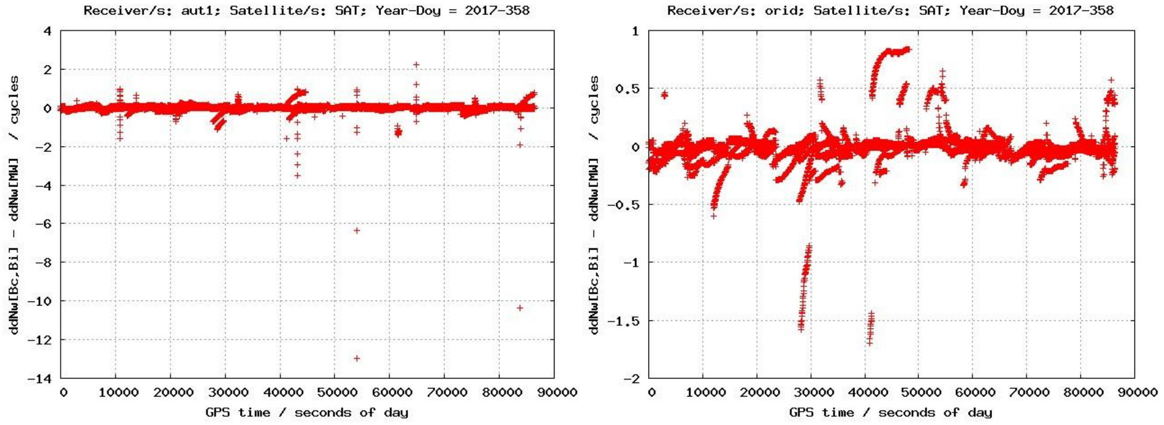

Figure 2.28 Difference of the double differenced widelane ambiguity, derived from the ionospheric-free and geometric-free double-differenced ambiguities, minus the value provided by the double-differenced ionospheric and geometric-free Melbourne-Wübbena combination, in cycles, versus time: left-hand plot correspond to the roving receiver AUT1 and the right-hand plot to the permanent receiver ORID, both during the second day of the RT experiment (day 24 December 2017).

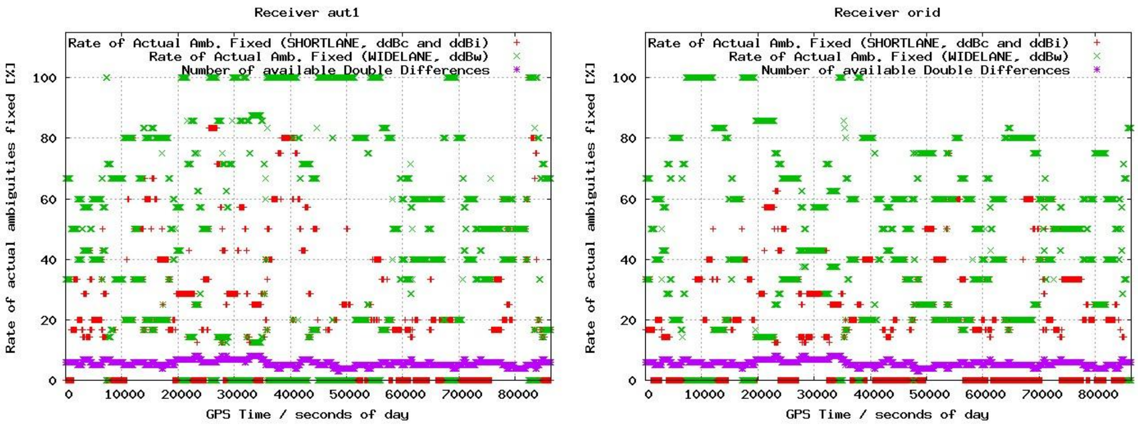

Figure 2.29 Percentage of RT double differenced carrier phase ambiguity fixing (widelane in green, narrowlane in red), and number of available double-differences (in magenta) are represented versus time: left-hand plot correspond to the roving receiver AUT1 and the right-hand plot to the permanent receiver ORID, both during the second day of the RT experiment (day 24 December 2017).

2.1.8 RT 3D-positioning error for the roving users (AUT1 and PVOG)

The positioning performance of both roving receivers, AUT1 and PVOG at 223 km and 465 km of the reference receiver SOFI (and at 196 km and 33 km from the closer reference receivers, respectively, ORID and KTCH) is shown in Figure 2.30, which can be compared when no ionospheric corrections and no corresponding user ambiguity fixing are used, in Figure 2.31. It is evident the much better performance of WARTK for both users, in general, in terms of convergence time (and final accuracy achieved) after each user cold start, compared when the ionospheric information is not used by the users. carrier-phase relative positioning technique. The exception happens since 43000 to about 70000 seconds for AUT1 (and up to 54000 for PVOG), coinciding with the anomalous high residuals in the spatially linear VTEC fitting per satellite (Figure 2.18), but not clearly seen in the ambiguity fixing information shown in Figure 2.28 and Figure 2.29. A summary of the performance in convergence time and final accuracy, achieved when using or not ionospheric corrections, can be seen in Figure 2.33 (AUT1) and Figure 2.34 (PVOG). It can be seen that the most part of the convergence time happens before 600 seconds, and a majority before 200 seconds, versus 5500 and 2000 seconds respectively without ionospheric corrections. This means one order of magnitude in the reduction of the convergence time. The final accuracy is typically below 5 cm with WARTK and below 15 cm for the most distant roving user AUT1 (and below 10 cm for PVOG) without ionospheric corrections.

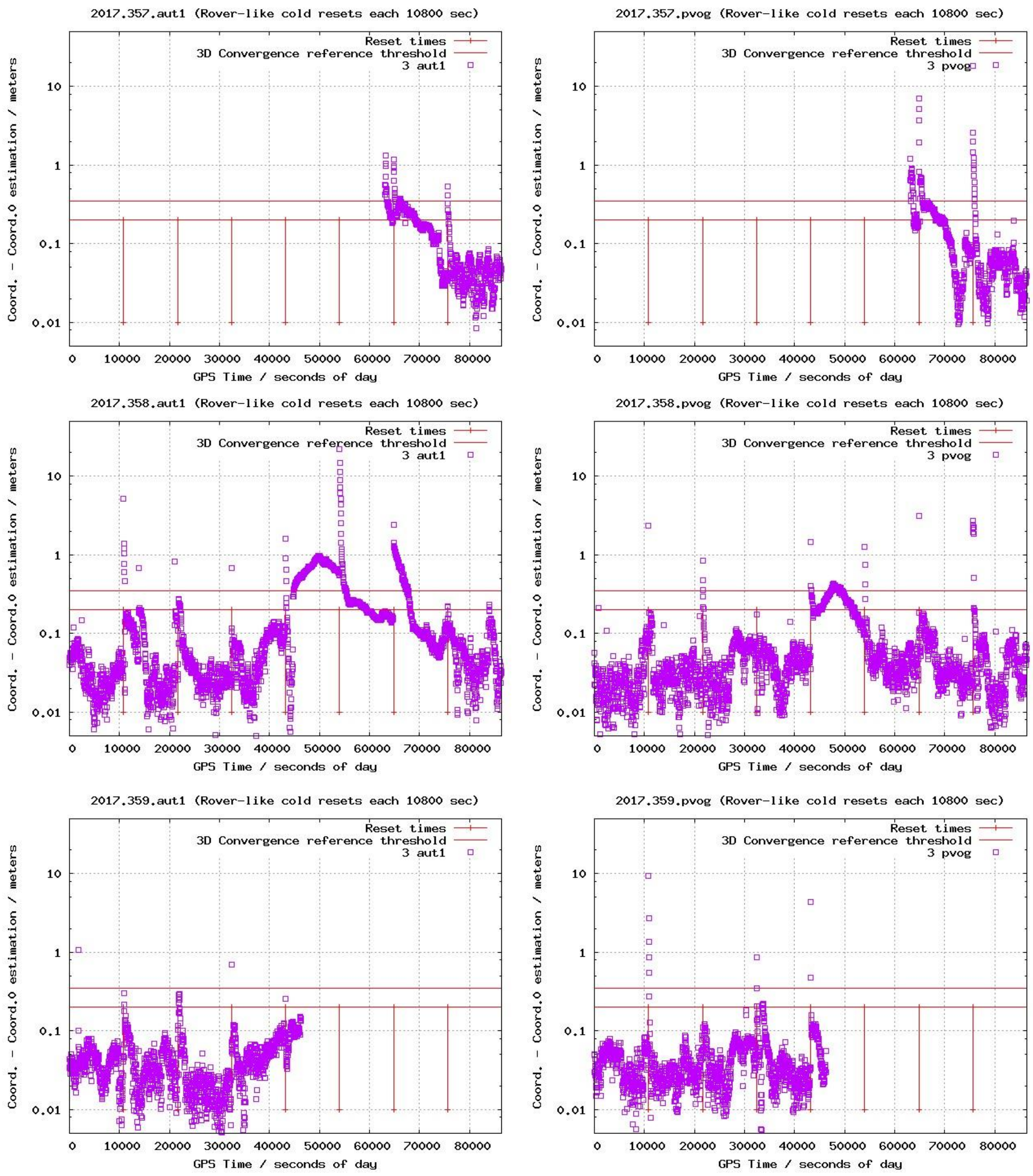

2017.357.aut1 (Rover-like cold resets each 10800 sec)

2017.357.pvog (Rover-like cold resets each 10800 sec)

2017.358.aut1 (Rover-like cold resets each 10800 sec)

2017.358.pvog (Rover-like cold resets each 10800 sec)

2017.359.aut1 (Rover-like cold resets each 10800 sec)

2017.359.pvog (Rover-like cold resets each 10800 sec)

Figure 2.30 3D RT positioning error of the WARTK (i.e. fixing wide- and narrow-lane ambiguities) roving GPS receivers AUT1 (first column) and PVOG (second column) during the overall Christmas days experiment (days 23, 24 and 25 December 2017, in first, second and third row respectively).

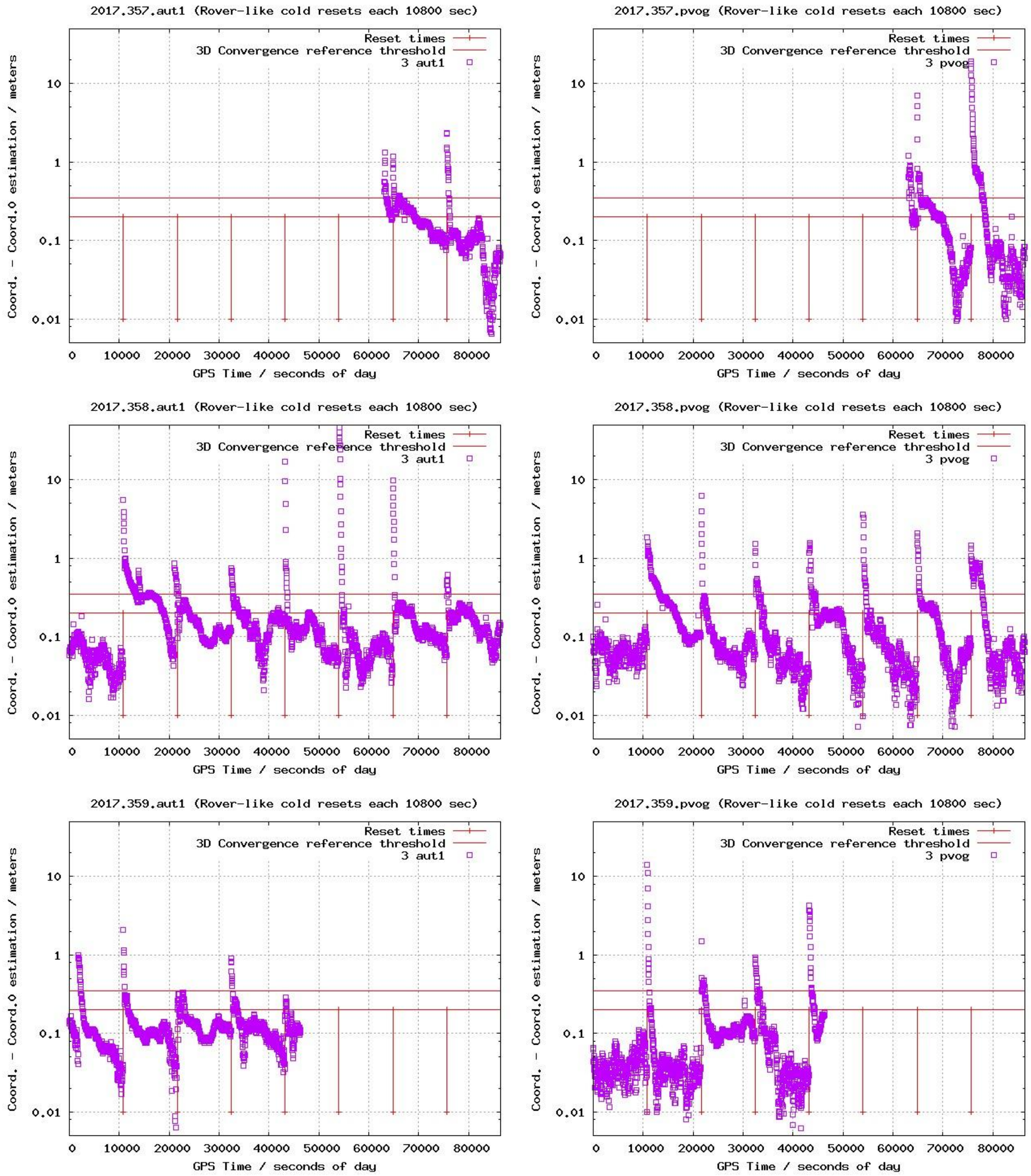

Figure 2.31 3D RT carrier-phase based differential positioning error (i.e. no fixing carrier phase ambiguities) for the roving GPS receivers AUT1 (first column) and PVOG (second column) during the overall Christmas days experiment (days 23, 24 and 25 December 2017, in first, second and third row respectively).

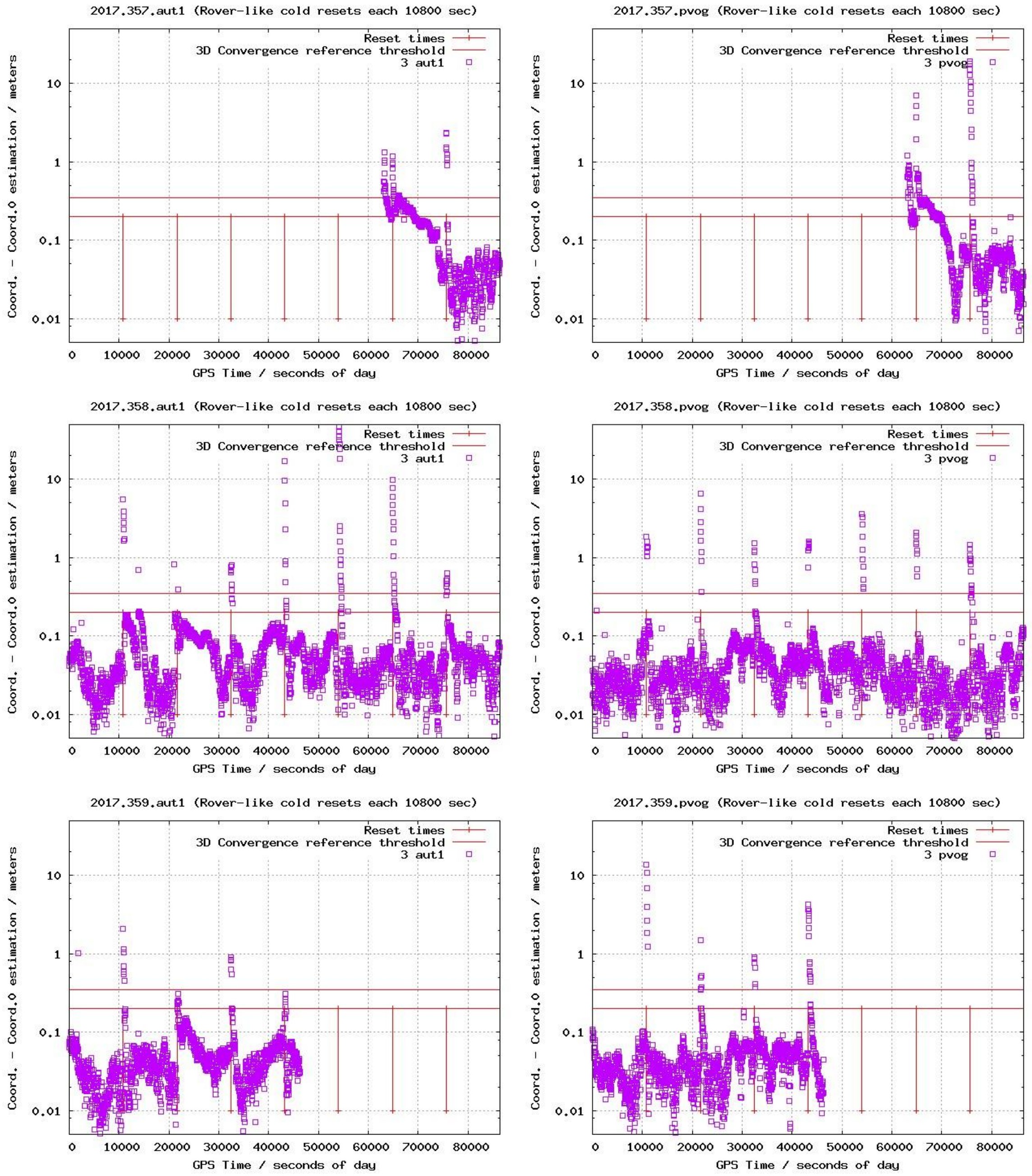

Figure 2.32 3D RT carrier-phase based differential positioning error (i.e. fixing wide- and narrow-lane ambiguities, with higher requirements of bias error estimates to fix both double-differences) for the roving GPS receivers AUT1 (first column) and PVOG (second column) during the overall Christmas days experiment (days 23, 24 and 25 December 2017, in first, second and third row respectively).

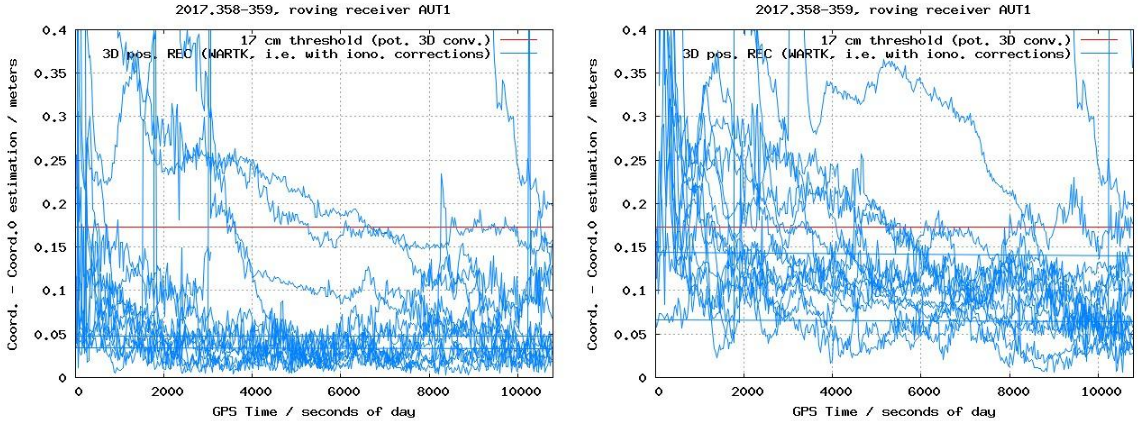

Figure 2.33 3D RT positioning error for roving receiver AUT1 with WARTK (i.e. constraining the wide- and narrow-lane ambiguities with the ionospheric corrections, left) and without ionospheric corrections, i.e. without constraining the ambiguities (right), during the overall Christmas days experiment (days 23, 24 and 25 December 2017).

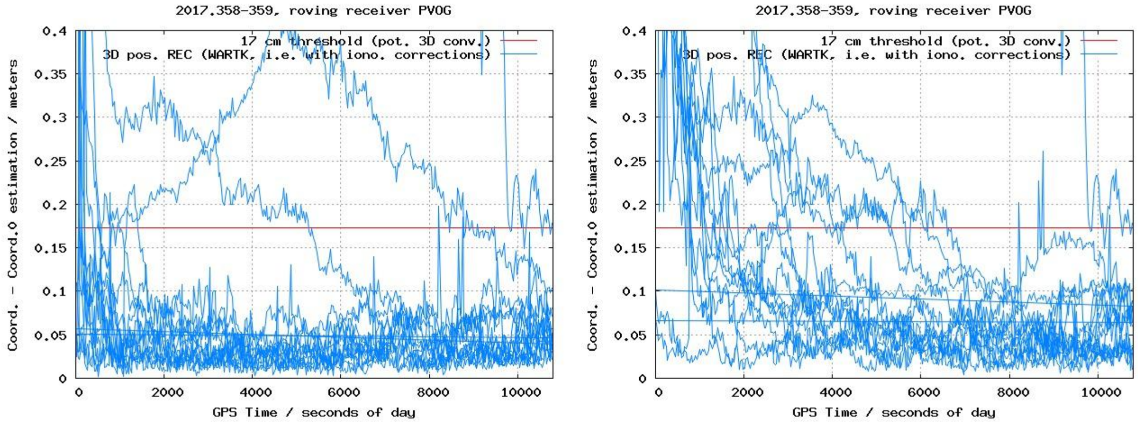

Figure 2.34 3D RT positioning error for roving receiver PVOG with WARTK (i.e. constraining the wide- and narrow-lane ambiguities with the ionospheric corrections, left) and without ionospheric corrections, i.e. without constraining the ambiguities (right), during the overall Christmas days experiment (days 23, 24 and 25 December 2017).

2.1.9 Trying to clarify the reason of the temporarily WARTK worsening starting 43200 sec of day 358, 2017: Single Receiver MSTID Index and MSTID footprints

In order to try to identify and understand the potential reasons of the RT positioning performance decrease for roving users during the central day (since 43000 to about 70000 seconds for AUT1, and up to 54000 for PVOG, day 358, 2017), coinciding with the sudden increase of CPF ionospheric planar fit residuals per satellite, as shown above, we have computed the Single Receiver MSTID activity index, SRMTID. This has been done after performing a first analysis of the post-fit residuals of the five measurements without providing new insights (see Appendix). Indeed, the SRMTID index will help us to confirm the suspicious of significant activity coinciding with the period of WARTK poorest performance, based in some of our previous works (such as Hernández-Pajares et al. 2012). Indeed, it can be seen in Figure 2.35 that this is the case, coinciding with the climatic occurrence of MSTID at mid latitudes studied in the above mentioned reference (happening mainly on fall and winter daylight time, equatorward, and spring and summer night time, westward). A zoom showing up the effect of the MSTIDs around 42000-44000 seconds can be seen in Figure 2.36 with oscillations of about 10 cm in different phase for the four carrier phase measurements involved in the double-differenced, i.e. not cancelling, on the contrary when the double-differences of the ionospheric delays are considered. This non-linear of up to few decimeters is much larger than the maximum allowable error of the ionospheric correction (about 1.3 cm when the ambiguity parity check is used), strongly suggesting the possibility of bad ambiguity fixing behind such worse WARTK behaviour during day time coinciding with the MSTID activity. In order to mitigate this effect different techniques can be applied in future updates of the CPF, depending on the density of the network, being Hadasz et al. 2017 or Hernández-Pajares et al. 2012 ([9], [4]) more suitable for our sparse network, compared with Yang et al. 2017 for dense networks. In the mean time we have applied a more demanding condition to fix ambiguities, in terms of a reduction of the maximum allowable estimated error for Bi, ddBi, MW and ddMW, and it works quite well, eliminating the bad fixing during the center of day 358.

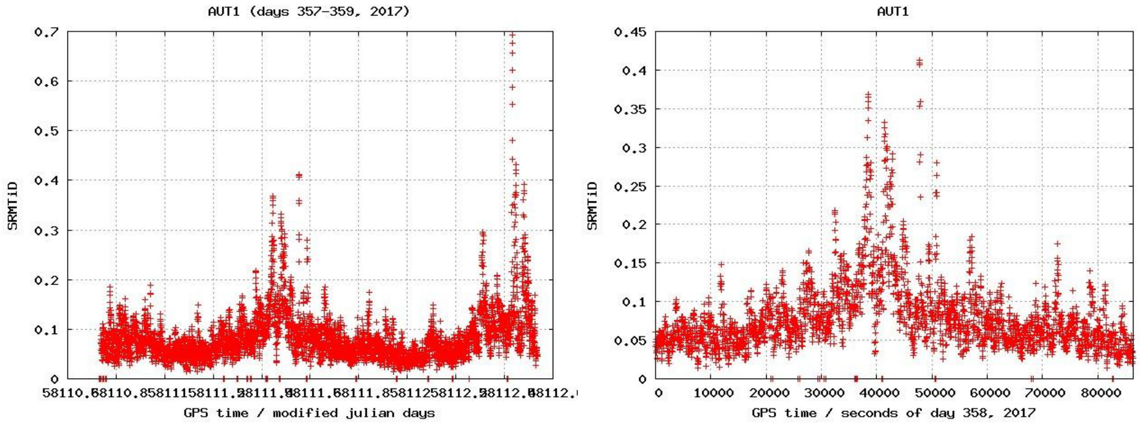

Figure 2.35 Single Receiver MSTID Index for roving receiver AUT1, versus time in Julian days for the overall RT experiment (left-hand plot) and versus seconds of day 358, 2017 (central day of the RT experiment).

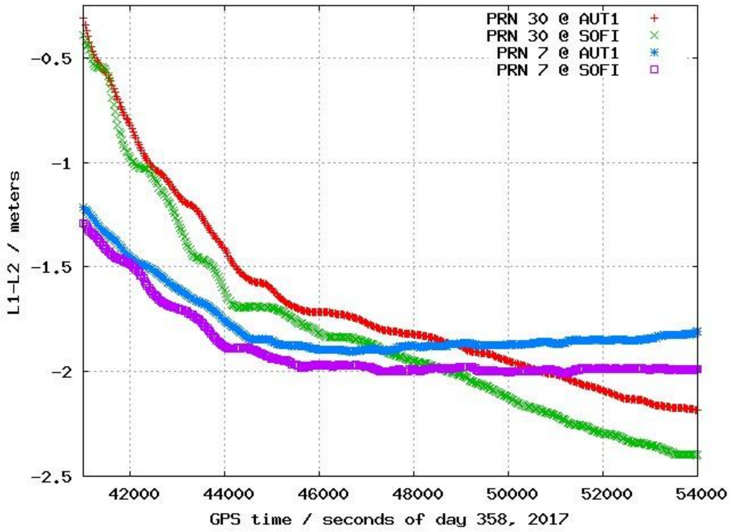

Figure 2.36 Zoom of Li=L1-L2 carrier phase measurements in length units for satellite PRN07 and PRN30 taken from receivers AUT1 and SOFI during 24 December, 2017.

2.1.10 Reprocessing by mitigating the MSTID effect on the temporarily WARTK worsening starting 43200 sec of day 358, 2017, by means of a more exigent threshold for the estimated standard deviation of the computed ionospheric carrier phase ambiguity corresponding to the WARTK user.

In order to improve the user RT positioning performance during the noon of the second day, when MSTID activity is important, we have implemented a simple update in the real-time filter: to be much more exigent to fix the ambiguities. Indeed, the maximum allowed standard deviation to fix has been change to, simultaneously, 15 cm, 25 cm and 2.7 cm for undifferenced widelane estimated ambiguity, the corresponding double differenced one, and the undifferenced ionospheric-combination ambiguity respectively (instead of 1m, 2m and 20cm respectively, as before). The improvement is clear: the long lasting time with high residuals of STEC planar fit per satellite during noon time go down to normal values (see Figure 2.37 and Figure 2.38) and the positioning error go down to normal values after convergence (typically below 10 cm, see Figure 2.39 and Figure 2.40). The "price to pay" is a not so strong reduction of the convergence time: the most part of ambiguities for WARTK user further from the permanent receivers, AUT1, need up to ~4000 seconds to convergence with no ionospheric corrections / ambiguity fixing; up to ~200 seconds with the previous most relaxed ambiguity fixing threshold; and up to ~500 seconds with the new parameters fixing the problems during the noon (see Figure 2.41). A similar relative situation is shown in the same figure for closer receiver PVOG, but with convergence values smaller as expected (especially in the case of non-use of ionospheric corrections).

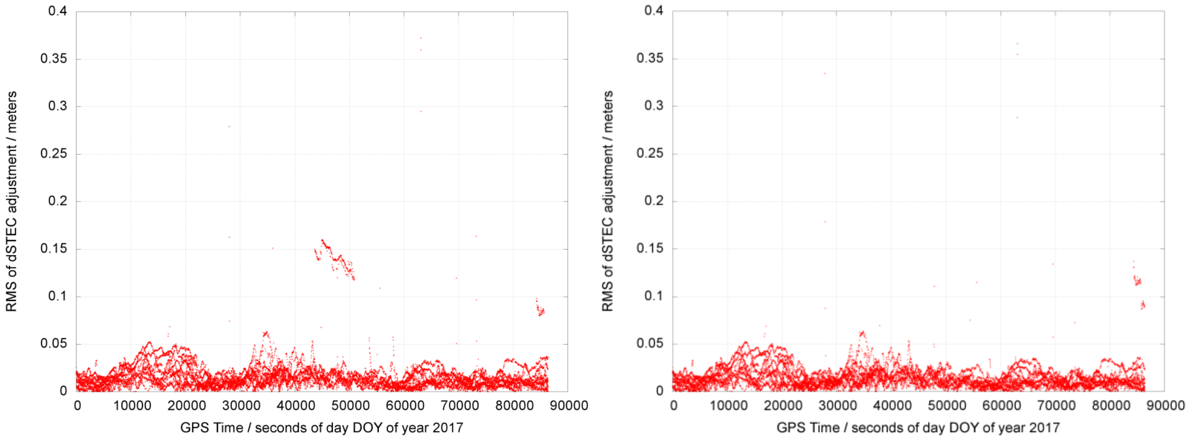

Figure 2.37 The RMS of the residuals of the VTEC fitting per satellite (vertical axis in meters of LI=L1-L2) vs time (horizontal axis in seconds of the day) is represented, during the second day of the RT experiment (day 24 December 2017), with the initial set of thresholds for user carrier phase ambiguity fixing (left) and with a more exigent one (right).

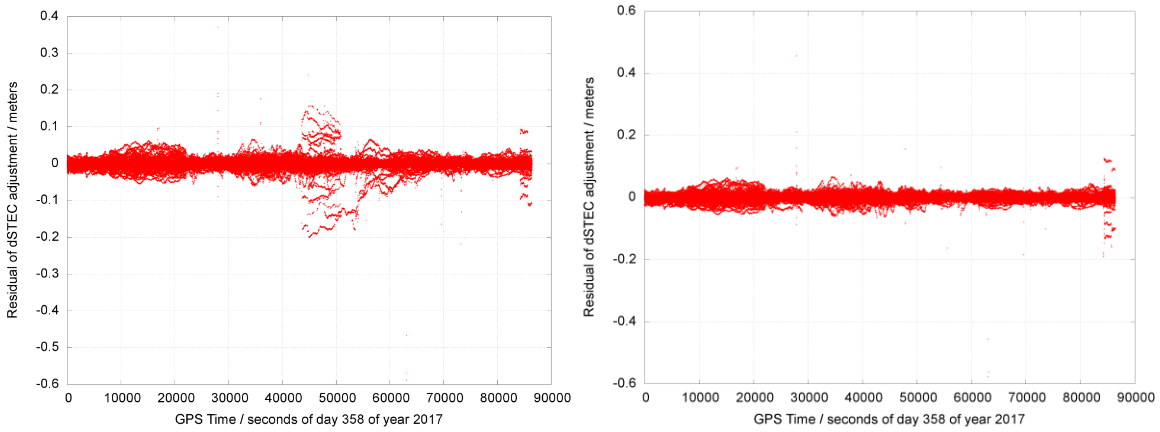

Figure 2.38 Residuals of the VTEC fitting per satellite (vertical axis in meters of LI=L1-L2) vs time (horizontal axis in seconds of the day) is represented, during the second day of the RT experiment (day 24 December 2017), with the initial set of thresholds for user carrier phase ambiguity fixing (left) and with a more exigent one (right).

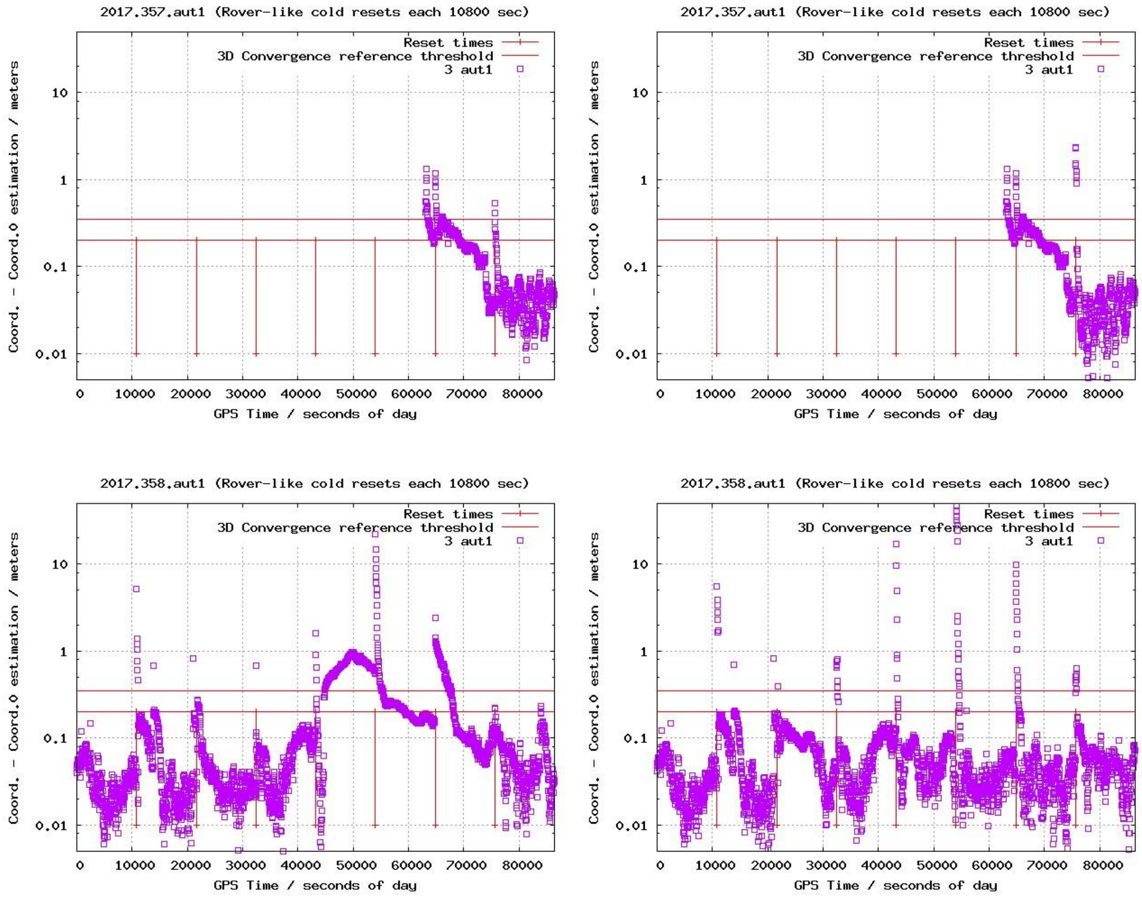

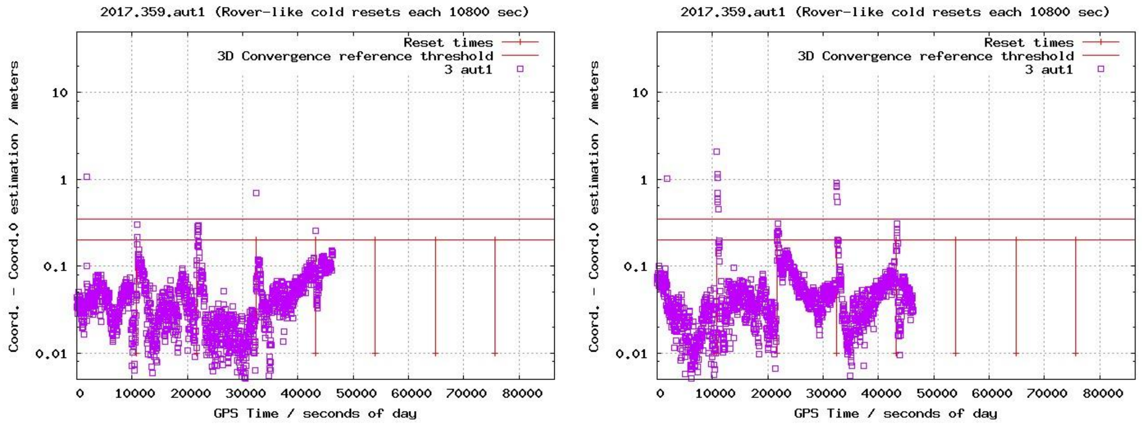

Figure 2.39 3D RT positioning error of the WARTK (i.e. fixing wide- and narrow-lane ambiguities) roving GPS receivers for AUT1 with previous threshold for ambiguity fixing (first column) and with the most exigent one (second column) during the overall Christmas days experiment (days 23, 24 and 25 December 2017, in first, second and third row respectively).

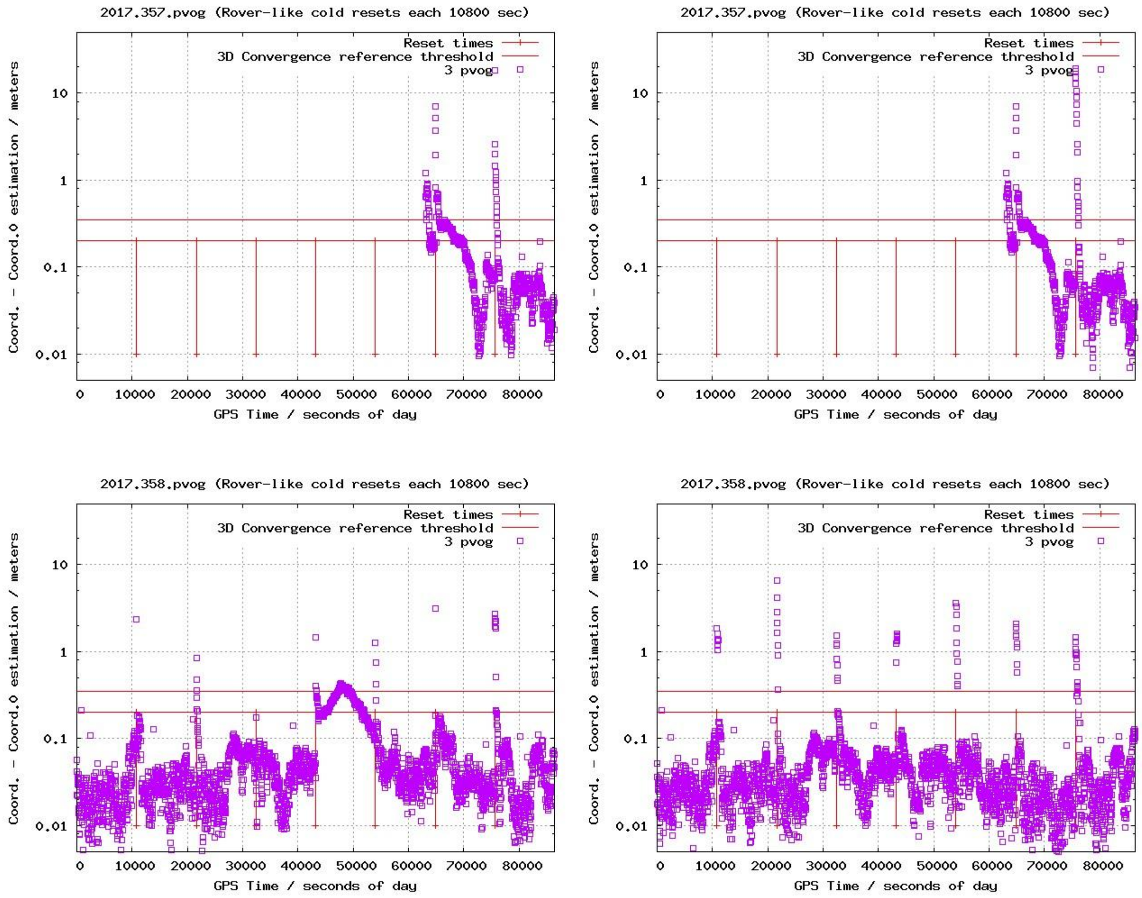

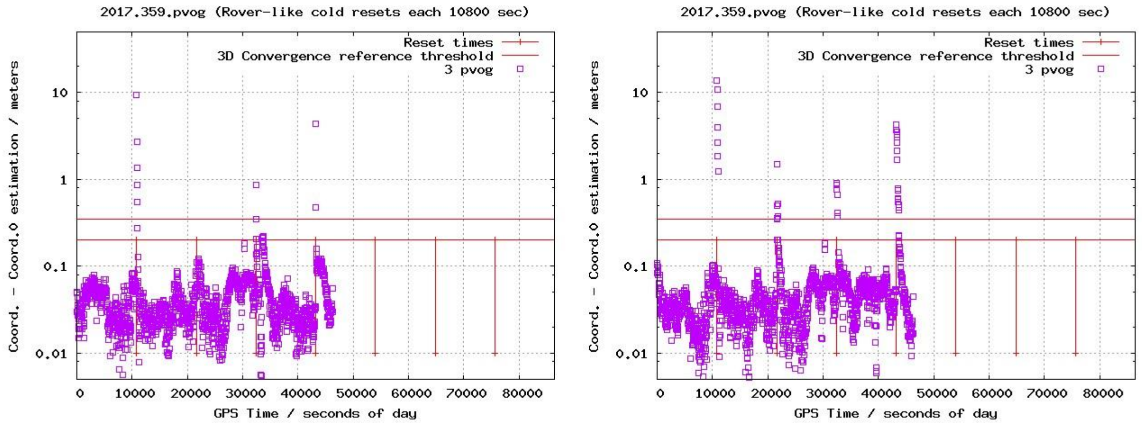

Figure 2.40 3D RT positioning error of the WARTK (i.e. fixing wide- and narrow-lane ambiguities) roving GPS receivers for AUT1 with previous threshold for ambiguity fixing (first column) and with the most exigent one (second column) during the overall Christmas days experiment (days 23, 24 and 25 December 2017, in first, second and third row respectively).

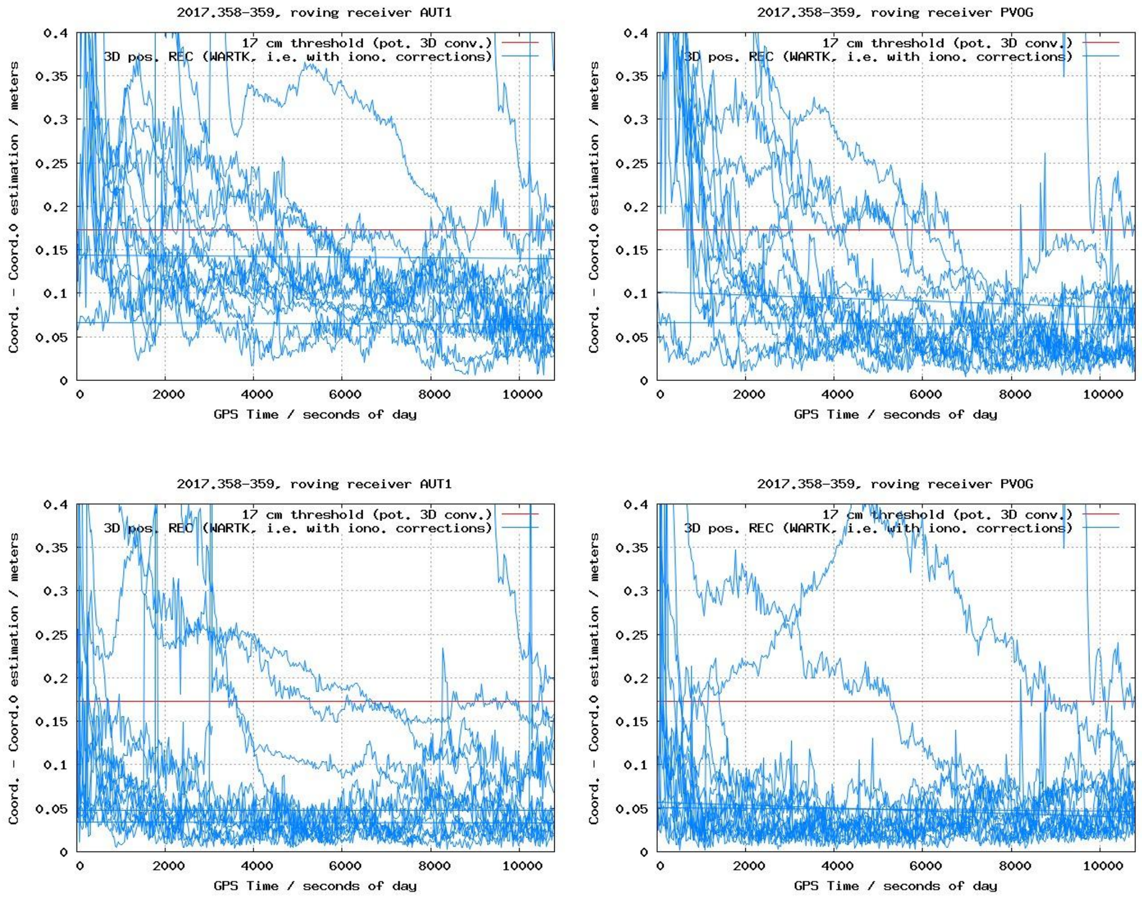

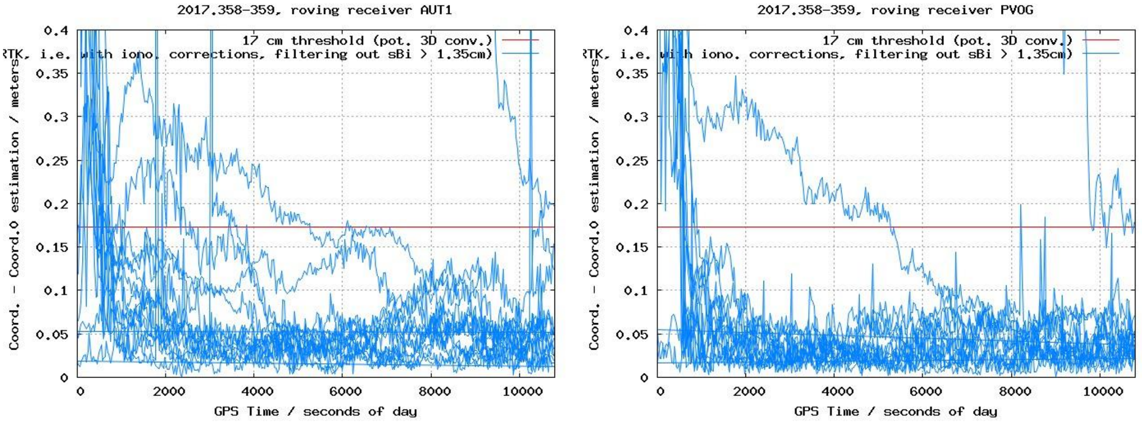

Figure 2.41 3D RT positioning error for roving receiver AUT1 (first column) and PVOG (second column), without ionospheric corrections i.e. without constraining the ambiguities (first row), with WARTK (i.e. constraining the wide- and narrow-lane ambiguities with the ionospheric corrections) in second row (former threshold for widelane and narrowlane ambiguity fixing) and in third row (for new more exigent ambiguity fixing thresholds), during the overall Christmas days experiment (days 23, 24 and 25 December 2017).

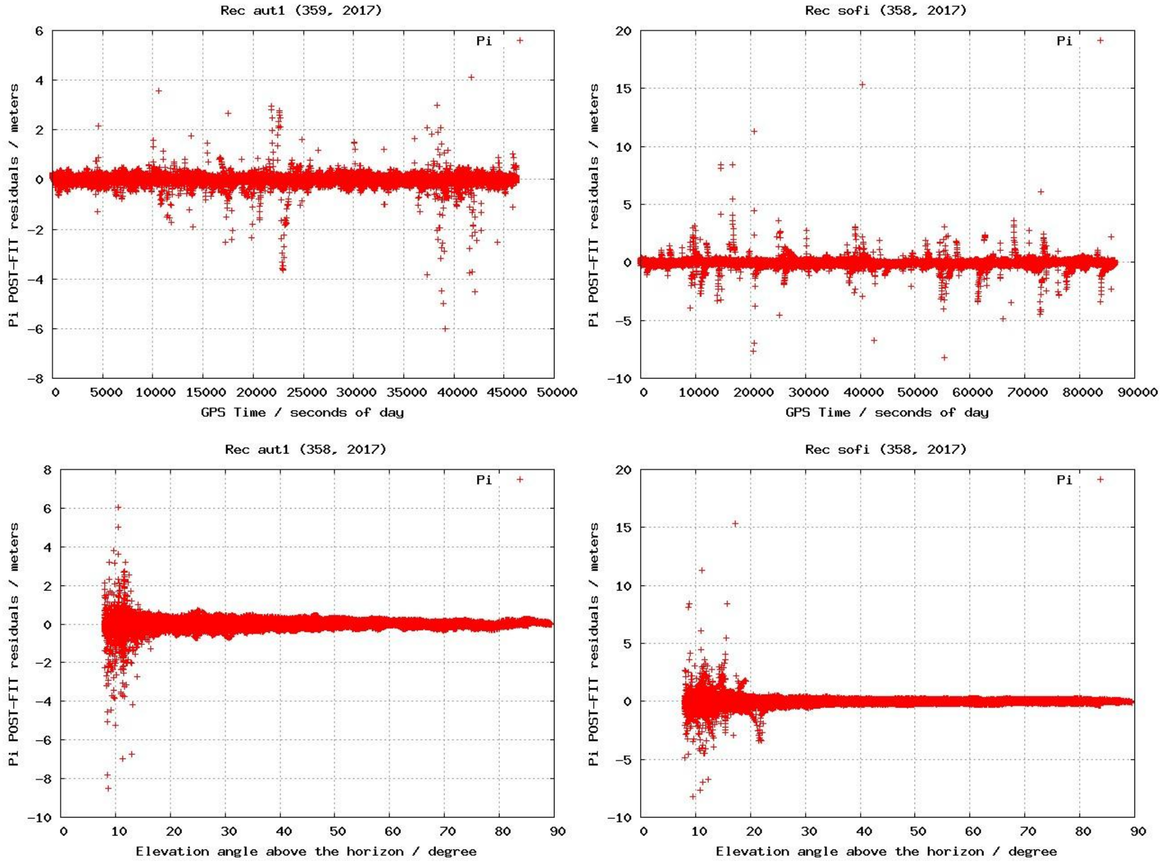

Figure 2.42 Post-fit residual for the ionospheric combination of the pseudoranges corresponding to the roving receiver AUT1 (first column) and the reference receiver SOFI (second column), versus time (first row) and versus elevation (second row), during day 25 December 2017.

3 AUDITOR corrections dissemination

3.1 VTEC dissemination via RTCM 1264

3.1.1 Process overview

The implemented VTEC dissemination data flow is as shown in Figure 3.1.

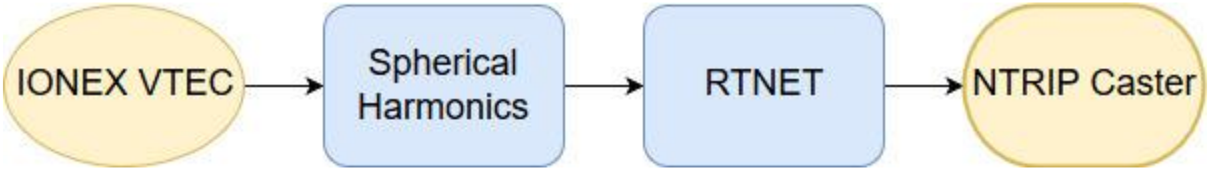

Figure 3.1 VTEC dissemination flow chart

The process uses as input a VTEC map in IONEX format [reference]. This map is then transformed in spherical harmonics to be compatible with the RTCM standard 1264 message. Afterwards, these data are transformed to a RTNET message. This is done because in this way we could use the BNC (BKG NTRIP Client) software to encode and send RTCM 1264 messages to a NTRIP caster. Doing so we could use this well-known, extensively tested and used software to manage the connection with the NTRIP caster. The VTEC data is then sent continuously at a 10 seconds period rate, to lower the wait time for a cold-start client.

3.1.2 Implementation description

All the process is done by a single python script (*ionex_2_bnc_rtnet.py*). Still, a set of bash scripts have been created to manage some system-related functions, configure the entire process and perform some minor system-related functions.

In this sense, the main bash script (*ionex_2_rtcm.sh*) consists of three sub-processes:

- Link creation: a first process is launched to continuously create a soft-link to the latest available IONEX file.
- IONEX to RTNET: a second process configures and launches the python script responsible of performing the tasks described earlier in this section: checking the IONEX file for updates, translating the VTEC data to RTNET and sending it in each configured time interval to the BNC software.
- BNC NTRIP server: a third process launches a BNC instance, which receives through an IP port the RTNET data and relies it to the NTRIP caster. In case the BNC process dies, it is automatically restarted again.

This main script also stores the PID (Process IDentifiers) in a file to make it easier to stop the entire chain and sends the output of all the processes in a single log file.

The following configuration parameters have been defined (inside the *config.sh* file, see Figure 3.2):

- `ionex_file_path`: Path to the directory where the different IONEX files are generated.
- `ionex_iaac_name`: Name of the IAAC responsible to generate the ionex file. Used to find the correct ionex file to distribute.

- `spherical_harmonics_degree` and `spherical_harmonics_order`: Maximum degree and order used for the spherical harmonics expansion. Must be equal or less than 15 to be compatible with RTCM 1264.
- `rtcm_message_period`: Time interval to send again the latest VTEC data.
- `bnc_ip`: IP used for the local bnc process acting as BNC server to receive the VTEC data to send to the caster.
- `bnc_port`: Port used for the local bnc process acting as BNC server. If set to 0, a random free port higher than 1024 (unprivileged ports) is used.
- `bnc_mountpoint`: Mountpoint name to transmit to the caster.
- `ntrip_server_*`: Various information sent to the caster about the NTRIP server. Some casters, like SNIP, do not implement sharing information about the server this way and then it will be simply ignored.
- `caster_ip`: IP of the NTRIP caster where to send the VTEC data.
- `caster_port`: Port of the NTRIP caster.
- `caster_password`: Password used to authenticate to the NTRIP caster.

```
ionex_file_path=/var/www/tomion/real-time/quick/last_results/
ionex_iaac_name="urtg"

spherical_harmonics_degree=15
spherical_harmonics_order=15

rtcm_message_period=10      #In seconds

bnc_ip='127.0.0.1'
bnc_port=0                  #0 to get a dynamically generated port
bnc_mountpoint="URTG"

ntrip_server_latitude=41.39
ntrip_server_longitude=2.15
ntrip_server_city="Barcelona"
ntrip_server_country="ESP"

caster_ip='127.0.0.1'
caster_port=2101
caster_password="<DELETED>"
```

Figure 3.2: Configuration used in the implementation of the VTEC dissemination

3.1.2.1 IONEX to RTNET processing

This is the process that performs all the computations. An overall flow chart can be seen at Figure 3.3. The process opens a TCP/IP socket and waits until the BNC client connects. Afterwards it enters an infinite loop, updating and sending the data.

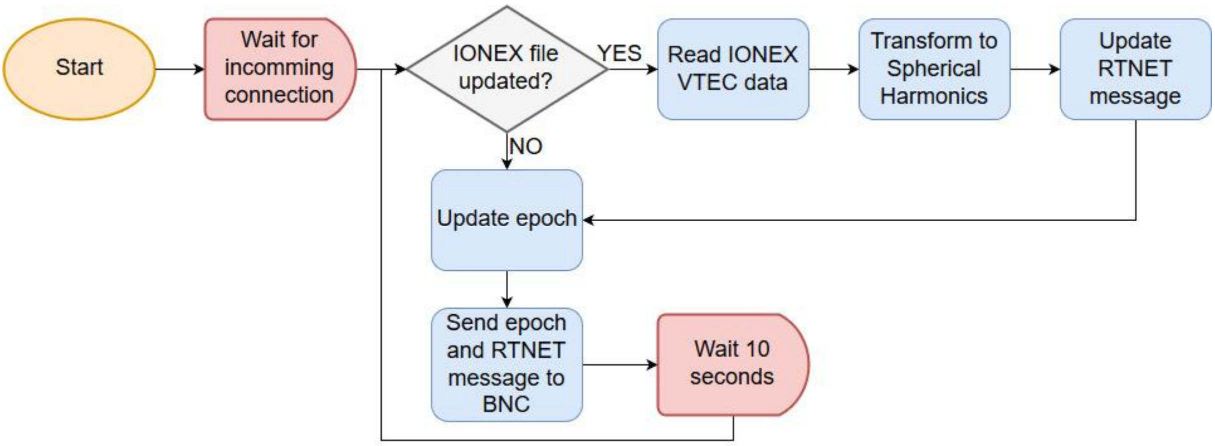

Figure 3.3 IONEX to BNC RTNET flow chart

The process uses as input a VTEC map in IONEX format. The MD5 hash is continuously computed over this file and when its value changes, the file is parsed again and the VTEC data of the last map available is used as the current map to be distributed to the clients. In the current tested implementation this map is the URTG (UPC Real-Time Global) GIM (Global Ionospheric Map). This GIM is computed by UPC and made publicly available free of charge through FTP on UPC servers and NASA's CDDIS, among others. Due to the computation time of the GIM, a latency of about 9 minutes exists between the station observables used as input for the GIM and the VTEC map. The effect of this delay on the quality of the VTEC data is considered negligible.

In case the IONEX file has been updated, two transformations are done. The first computational step of the implemented solution consists in transforming the VTEC map in an expansion of harmonics to be compatible with the RTCM standard 1264 message. The standard limits the maximum order and degree of the spherical harmonics to 15 both. This is currently the main source of error producing a smoothing of the VTEC map. The relative error of this step has been assessed to be around 6 % (see Roma-Dollase et al., 2017 [7], and next Section 3.2).

The second step consists in transforming the spherical harmonics to a RTNET message. In this step, an additional rounding to the nearest even value is performed following the IEEE floating point standard. This rounding is needed since the RTCM 1264 standard has a resolution for the coefficients of 0.005 TECU. The error introduced by this step is considered negligible since the dominant lower order and degree coefficients have much larger values and hence it only affects the less important coefficients with small values.

Finally, every 10 seconds, the epoch information of the RTNET message is updated and the latest RTNET message is sent to the BNC socket.

3.1.3 Execution

The entire process has been running in production at a server in UPC. During the tests of this implementation, some issues have been raised and solved, all of them related to the asynchrony between the GIM generation and the dissemination process. For example, when the day changes the file of the previous date is moved to another location and some time passes before the new file is available. In this case, the hash computation of the file failed since the file did not exist and the updating of the VTEC data was halted until the new file appeared. In another case, it was detected that sometimes the IONEX file parsing failed. This was since the IONEX file was read while the GIM generation process was still writing it. This was also solved, and now in case the IONEX file parsing fails the previous VTEC data is also used. It is to notice that in both cases only the updating of the VTEC data sent to BNC is halted, the sending of the data itself still is done at the frequency defined.

The full chain has been validated using SNIP software (Figure 3.4) as NTRIP caster and another BNC instance as NTRIP client. This has been running, once the previous issues were solved, for more than 10 days uninterruptedly without any issue. It was also tested that even in the case that the NTRIP caster is not reachable, the dissemination process will automatically reconnect to the caster once it is working again.

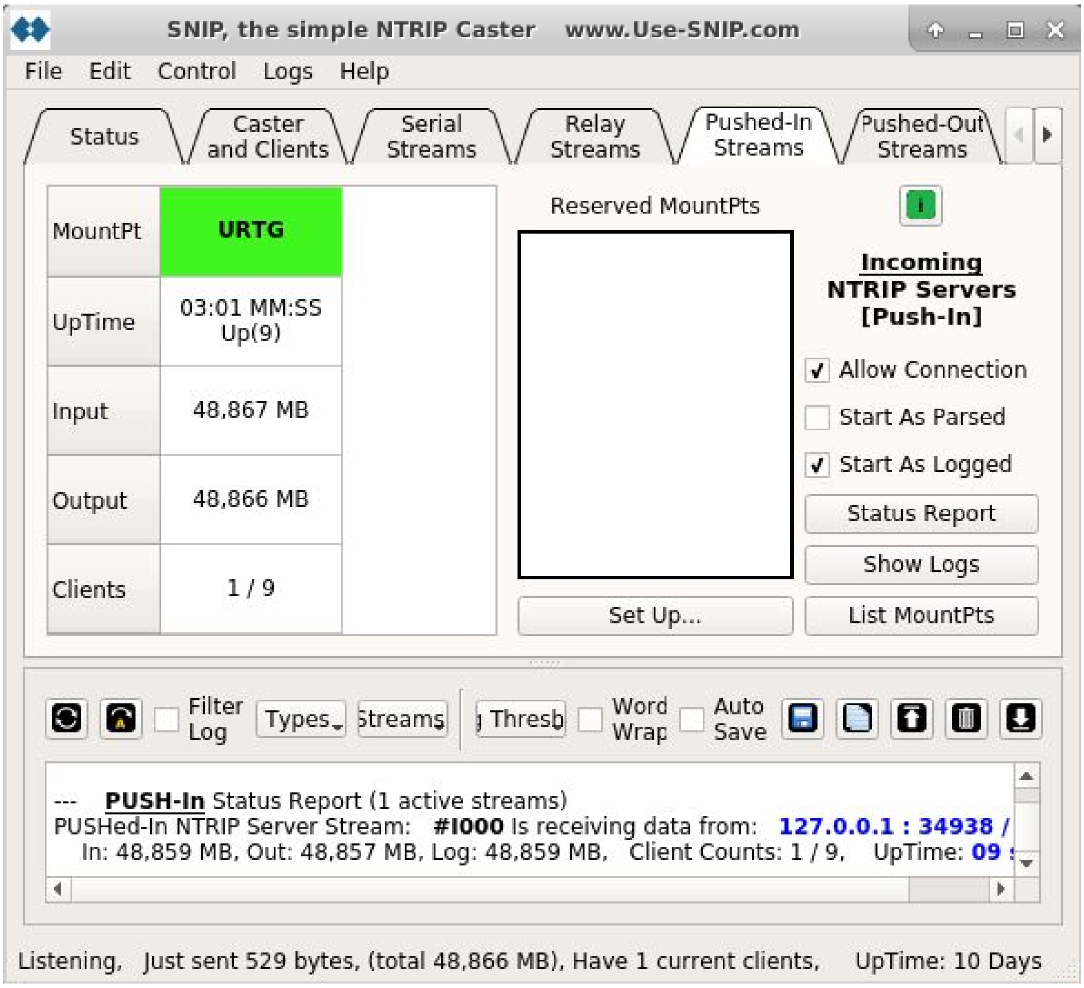

MountPt	URTG
UpTime	03:01 MM:SS Up(9)
Input	48,867 MB
Output	48,866 MB
Clients	1 / 9

☑ Allow Connection
☐ Start As Parsed
☑ Start As Logged
☐ Filter Log
☐ Word Wrap
☐ Auto Save

```
---    PUSH-In Status Report (1 active streams)
PUSHed-In NTRIP Server Stream:   #I000 Is receiving data from:   127.0.0.1 : 34938 /
   In: 48,859 MB, Out: 48,857 MB, Log: 48,859 MB,   Client Counts: 1 / 9,   UpTime: 09
```

```
Listening,   Just sent 529 bytes, (total 48,866 MB), Have 1 current clients,     UpTime: 10 Days
```

Figure 3.4 SNIP Caster used for testing the VTEC dissemination distributing URTG GIMs uninterruptedly for more than 10 days.

3.2 Study on RTCM 1264 messages

At the moment, RTCM only defines one way to provide VTEC information to users: as a spherical harmonic series of a given order and degree (message type 1264). To our knowledge, the maximum order and degree allowed by the standard is 16. The possibility to consider an RTCM message type with ionospheric data representing a grid has been under discussion by the RTCM working group, though seems not envisaged for the near future.

In this context, a study on the apparent limitation of these messages has been carried out by analyzing the loss of precision for the end user when using spherical harmonics instead of the IONEX content directly (Hernández-Pajares et al. 2017b [6]).

For this purpose, UQRG GIMs for one specific day have been encapsulated in spherical harmonics considering different degree/order. The results in Figure 3.5, Figure 3.6, Figure 3.7 and Figure 3.8 show the original VTEC GIM and the reconstructed VTEC GIMs for several spherical harmonics configurations.

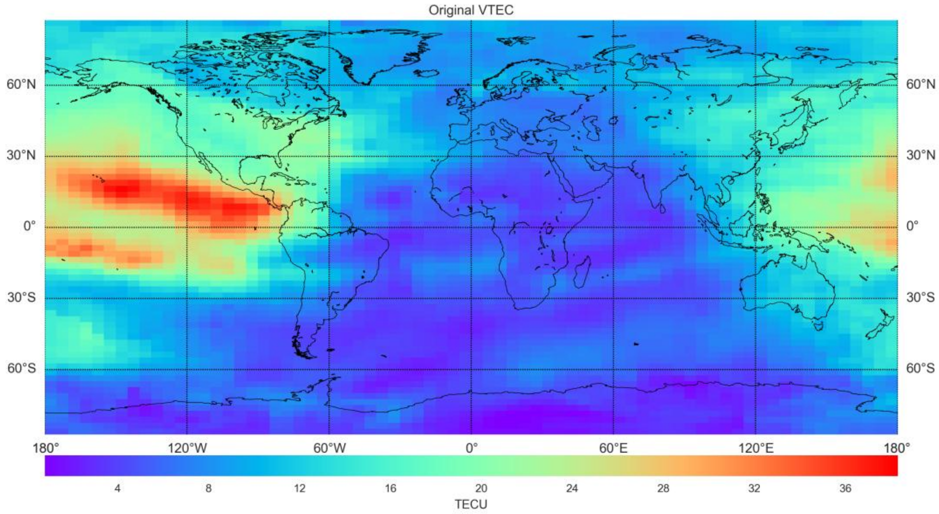

Figure 3.5 Original UQRG 15-minute VTEC GIM (UQRG1480.17i, 00UT)

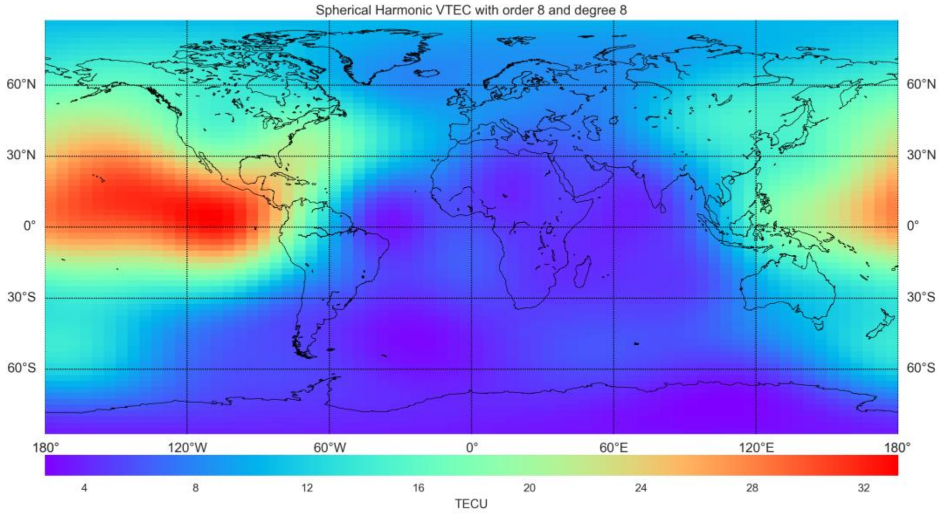

Figure 3.6 Reconstructed UQRG GIM considering SH of degree 8 and order 8, of day of year 148, 2017. Accounting for 13% RMS relative error.

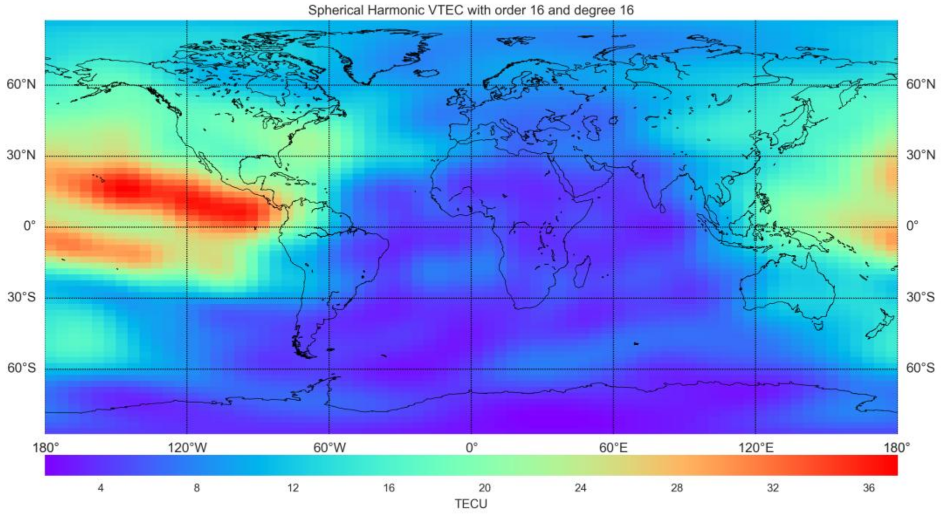

Figure 3.7 Reconstructed UQRG GIM considering SH of degree 16 and order 16, of day of year 148, 2017. Accounting for 5.8% RMS relative error.

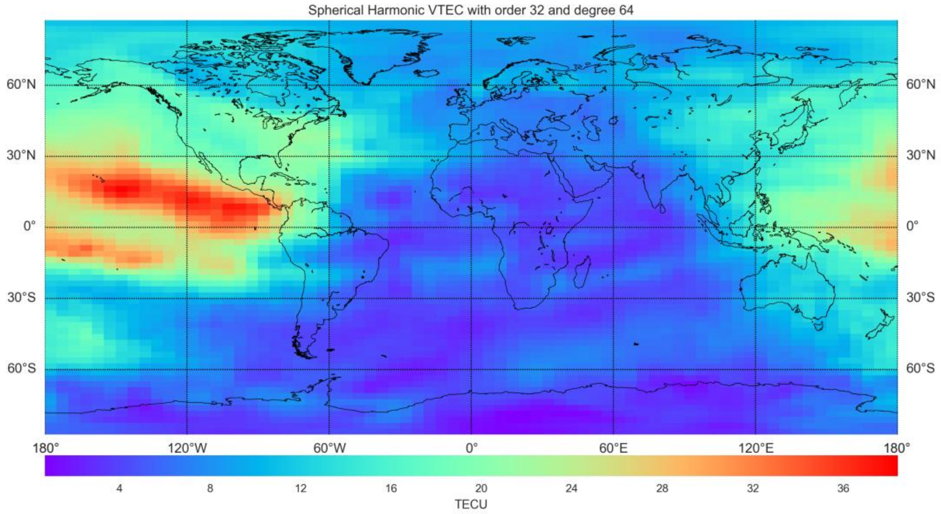

Figure 3.8 Reconstructed UQRG GIM considering SH of degree 64 and order 32, of day of year 148, 2017. Accounting for 1.8% RMS relative error.

3.2.1 Distribution of relative errors

More in detail, the following table provides the results for the multiple SH configurations (including the ones in the above Figures).

Table 3-1 RMS relative error in function of the SH degree/order for UQRG VTEC in day of year 148, 2017

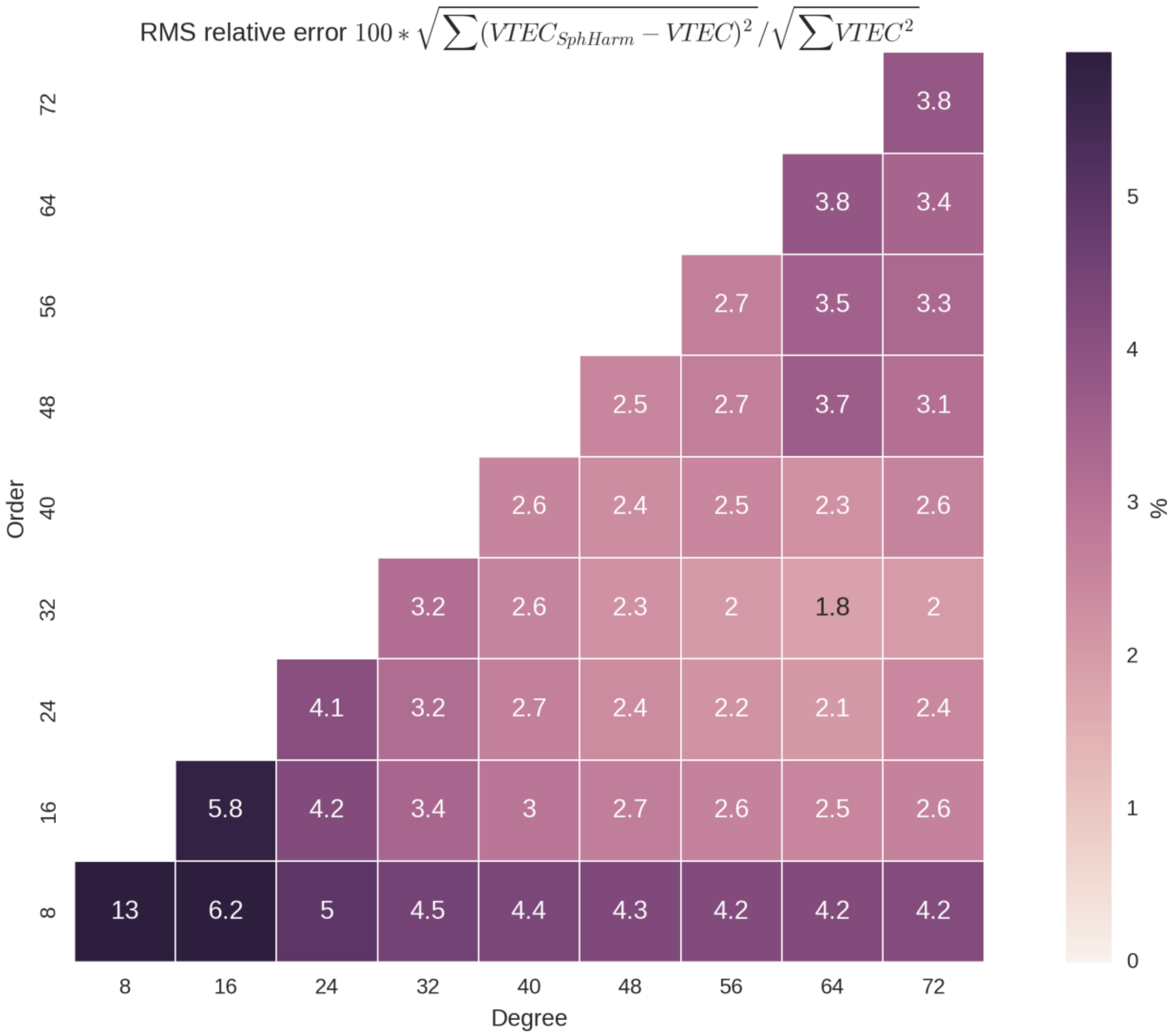

	8	16	24	32	40	48	56	64	72
72									3.8
64								3.8	3.4
56							2.7	3.5	3.3
48						2.5	2.7	3.7	3.1
40					2.6	2.4	2.5	2.3	2.6
32				3.2	2.6	2.3	2	1.8	2
24			4.1	3.2	2.7	2.4	2.2	2.1	2.4
16		5.8	4.2	3.4	3	2.7	2.6	2.5	2.6
8	13	6.2	5	4.5	4.4	4.3	4.2	4.2	4.2

3.3 DSM corrections / User observations dissemination via netcat

The possibility to disseminate DSM corrections has been finally tested using netcat as file server. Note that this approach is also valid for the dissemination of other types of information, such as the user observations to the CPF and the PVT data backwards, which will be finally implemented in AUDITOR.

For this purpose, we have considered the following Linux aliases to distinguish from other equivalent processes that could run in both the CPF server providing the corrections and another server emulating the user side.

alias AUDITORnc nc

alias AUDITORtail tail

In addition, we have defined a dedicated port for the dissemination of the corrections via netcat in both sides of the communication channel:

set AUDITORncport = 22216

On the sending end, located at chapman.upc.es server, it was required to run the following command lines:

```
cd ~/AUDITOR_DSM_netcat
alias AUDITORnc nc
alias AUDITORtail tail
AUDITORtail -f ~ionex4/art/AUDITOR-RT/messages1.output | grep ^DSM | AUDITORnc newg1.upc.es 22116 &
```

Note that the netcat execution at both sides is done as background processes so this allows to generate a permanent link between CPF and user sides.

On the destination end, which was tested at newg1.upc.es server, the following command lines were executed to validate the correct reception:

```
cd /d2/home/ionex4/AUDITOR_DSM_netcat
alias AUDITORnc nc
AUDITORnc -dlk 22116 > & DSM_incoming &
```

On the receiving end side, we are also listening on port 22116.

This concept was tested for the real-time distribution of DSM corrections in real-time, as provided by the CPF. The receiving end could receive the corrections without disruptions for 5 recent consecutive days. This approach will be implemented to establish the communication channel between the prototype AUDITOR receiver and the CPF.

4 AUDITOR GNSS-SDR with RTKLIB integration validation

GNSS-SDR now integrates the core RTKLIB libraries for Single Point Positioning and Precise Point Positioning. The user can configure the processing block in charge of PVT computation with a number of options, detailed hereafter:

Table 4-1 Configuration options for PVT computation in GNSS-SDR

Parameter	Description	Required
`implementation`	`RTKLIB_PVT`	Mandatory
`output_rate_ms`	Rate at which PVT solutions will be computed, in ms. It defaults to 500 ms.	Optional
`display_rate_ms`	Rate at which PVT solutions will be displayed in the terminal, in ms. It defaults to 500 ms.	Optional
`positioning_mode`	[`Single`, `PPP_Static`, `PPP_Kinematic`] Set positioning mode. `Single`: Single point positioning.`PPP_Static`: Precise Point Positioning with static mode. `PPP_Kinematic`: Precise Point Positioning for a moving receiver. It defaults to `Single`.	Optional
`num_bands`	[`1`: L1 Single frequency, `2`: L1 and L2 Dual-frequency, `3`: L1, L2 and L5 Triple-frequency] This option is automatically configured according to the Channels configuration. This option can be useful to force some configuration (*e.g.*, single-band solution in a dual frequency receiver).	Optional
`elevation_mask`	Set the elevation mask angle, in degrees. It defaults to 15º	Optional
`dynamics_model`	[`0`: Off, `1`: On] Set the dynamics model of the receiver. If set to 1 and `PVT.positioning_mode=PPP_Kinematic`, the receiver position is predicted with the estimated velocity and acceleration. It defaults to 0 (no dynamics model).	Optional
`iono_model`	[`OFF`, `Broadcast`, `Iono-Free-LC`]. Set ionospheric correction options. `OFF`: Not apply ionospheric correction. `Broadcast`: Apply broadcast ionospheric model. `Iono- Free-LC`: Ionosphere-free linear combination with dual frequency (L1-L2 for GPS or L1-L5 for Galileo) measurements is used for ionospheric correction. It defaults to `OFF` (no ionospheric correction)	Optional

Parameter	Description	Required
`trop_model`	[`OFF`, `Saastamoinen`, `Estimate_ZTD`, `Estimate_ZTD_Grad`]. Set whether tropospheric parameters (zenith total delay at rover and base-station positions) are estimated or not. `OFF`: Not apply troposphere correction. `Saastamoinen`: Apply Saastamoinen model. `Estimate_ZTD`: Estimate ZTD (zenith total delay) parameters as EKF states. `Estimate_ZTD_Grad`: Estimate ZTD and horizontal gradient parameters as EKF states. If defaults to `OFF` (no troposphere correction).	Optional
`code_phase_error_ratio_l1`	Code/phase error ratio R_r for the L1 band. It defaults to 100.	Optional
`carrier_phase_error_factor_a`	Carier phase error factor $a_{2\sigma}$. It defaults to 0.003 m.	Optional
`carrier_phase_error_factor_b`	Carier phase error factor $b_{2\sigma}$. It defaults to 0.003 m.	Optional
`slip_threshold`	Set the cycle-slip threshold (m) of geometry-free LC carrier-phase difference between epochs. It defaults to 0.05.	Optional
`threshold_reject_GDOP`	Set the reject threshold of GDOP. If the GDOP is over the value, the observable is excluded for the estimation process as an outlier. It defaults to 30.0.	Optional
`threshold_reject_innovation`	Set the reject threshold of innovation (pre-fit residual) (m). If the innovation is over the value, the observable is excluded for the estimation process as an outlier. It defaults to 30.0 m.	Optional
`number_filter_iter`	Set the number of iteration in the measurement update of the estimation filter. If the baseline length is very short like 1 m, the iteration may be effective to handle the nonlinearity of measurement equation. It defaults to 1.	Optional
`sigma_bias`	Set the process noise standard deviation of carrier-phase bias σ_{bias}, in cycles/$\sqrt{s}$. It defaults to 0.0001 cycles/$\sqrt{s}$.	Optional
`sigma_trop`	Set the process noise standard deviation of zenith tropospheric delay σ_z, in m/$\sqrt{s}$. It defaults to 0.0001 m/$\sqrt{s}$.	Optional
`raim_fde`	[`0`, `1`]: Set whether RAIM (receiver autonomous integrity monitoring) FDE (fault detection and exclusion) feature is enabled or not. It defaults to 0 (RAIM not enabled)	Optional

Parameter	Description	Required
`reject_GPS_IIA`	[`0`, `1`]: Set whether the GPS Block IIA satellites are excluded or not. Those satellites often degrade the PPP solutions due to unpredicted behavior of yaw-attitude. It defaults to 0 (no rejection).	Optional
`phwindup`	[`0`, `1`]: Set whether the phase windup correction ϕ_{pw} for PPP modes is applied or not. It defaults to 0 (no phase windup correction).	Optional
`earth_tide`	[`0`, `1`]: Set whether earth tides correction is applied or not. If set to 1, the solid earth tides correction $d_{r,disp}$ is applied to the PPP solution, following the description in IERS Technical Note No. 32[3], Chapter 7. It defaults to 0 (no Earth tide correction).	Optional
`rinex_version`	[`2`: version 2.11, `3`: version 3.02] Version of the generated RINEX files. It defaults to 3.	Optional
`nmea_dump_filename`	Name of the file containing the generated NMEA sentences in ASCII format. It defaults to `./nmea_pvt.nmea`.	Optional
`flag_nmea_tty_port`	[`true`, `false`]: If set to `true`, the NMEA sentences are also sent to a serial port device. It defaults to `false`.	Optional
`nmea_dump_devname`	If `flag_nmea_tty_port` is set to `true`, descriptor of the serial port device. It defaults to `/dev/tty1`.	Optional
`flag_rtcm_server`	[`true`, `false`]: If set to `true`, it runs up a TCP server that is serving RTCM messages to the connected clients during the execution of the software receiver. It defaults to `false`.	Optional
`rtcm_tcp_port`	If `flag_rtcm_server` is set to `true`, TCP port from which the RTCM messages will be served. It defaults to 2101.	Optional
`rtcm_station_id`	Station ID reported in the generated RTCM messages. It defaults to 1234.	Optional
`rtcm_MT1045_rate_ms`	Rate at which RTCM Message Type 1045 (Galileo Ephemeris data) will be generated, in ms. If set to `0`, mutes this message. It defaults to 5000 ms.	Optional
`rtcm_MT1019_rate_ms`	Rate at which RTCM Message Type 1019 (GPS Ephemeris data) will be generated, in ms. If set to `0`, mutes this message. It defaults to 5000 ms.	Optional
`rtcm_MSM_rate_ms`	Default rate at which RTCM Multiple Signal Messages will be generated. It defaults to 1000 ms.	Optional

Parameter	Description	Required
`rtcm_MT1077_rate_ms`	Rate at which RTCM Multiple Signal Messages GPS MSM7 (MT1077 - Full GPS observations) will be generated, in ms. If set to `0`, mutes this message. It defaults to `rtcm_MSM_rate_ms`.	Optional
`rtcm_MT1097_rate_ms`	Rate at which RTCM Multiple Signal Messages Galileo MSM7 (MT1097 - Full Galileo observations) will be generated, in ms. If set to `0`, mutes this message. It defaults to `rtcm_MSM_rate_ms`.	Optional
`flag_rtcm_tty_port`	[`true`, `false`]: If set to `true`, the generated RTCM messages are also sent to a serial port device. It defaults to `false`.	Optional
`rtcm_dump_devname`	If `flag_rtcm_tty_port` is set to `true`, descriptor of the serial port device. It defaults to `/dev/pts/1`.	Optional
`dump`	[`true`, `false`]: If set to `true`, it enables the PVT internal binary data file logging. It defaults to `false`.	Optional
`dump_filename`	If `dump` is set to `true`, name of the file in which internal data will be stored. It defaults to `./pvt.dat`.	Optional

The list of parameters in Table 4-1 includes those offered by RTKLIB's Graphical User Interface. Thus, users can make use of RTKLIB libraries for obtaining position fixes from GNSS-SDR without the need of installing both programs. The license in which the RTKLIB library is released (BSD 2-clause license) allows the integration of the core library files into the GNSS-SDR source tree. Some modifications were made for the sake of code correctness and the easier integration within GNSS-SDR source tree structure and coding style, but in essence it is the same source code that comes with RTKLIB, and it obtains the same numerical results from the same input data.

5 Conclusions

A full and very realistic analysis of the performance of the AUDITOR WARTK CPF and user algorithms in actual real-time conditions during 23 to 25 December 2018, including two permanent receivers up to few hundred kilometres far treated as rover users with a cold starting up every 3 hours, is presented. The main conclusions are:

- The RT results obtained initially in actual real-time were quite good, especially in terms of a convergence time. This value is typically smaller than ~200 seconds, less than one order of magnitude smaller than the convergence time without ionospheric corrections (typically up to 4000 seconds). But there appear a significant positioning performance worsening at the noon of the second day.
- This user RT positioning worsening is coinciding with the existence of MSTIDs, the most frequent source of non-linearity affecting the precise ionospheric modelling in real-time.
- The problem in terms of positioning error is eliminated when the maximum formal ambiguity error threshold for user ambiguity fixing is strongly reduced, as a simple mitigation way of the MSTID effect in particular when the estimated error of the user' ionospheric-combination phase ambiguities are considered.

  A slight worsening found in term of user precise positioning convergence time with the new user ambiguity thresholds (about double, up to ~400 seconds typically of convergence time) might be mitigated in the future by adopting some of the RT MSTID modelling techniques conceived by the authors of this report (Hernández-Pajares et al. 2012 [4], Hadas et al. 2017 [9], Yang et al. 2017 [8]).

Regarding the dissemination of AUDITOR data, we have implemented a VTEC dissemination data flow by means of the standard RTCM message type 1264, which is based on Spherical Harmonics of a given order and degree. In this context, a study was conducted on the loss of precision for the end user when using spherical harmonics instead of the IONEX content directly.

Secondly, the possibility to transmit STEC correction messages from the CPF (in DSM format) without any loss of precision has been tested using netcat (nc) computer networking utility as file server. This approach can also be suitable to transmit the observations from the user side to the CPF and the PVT data from the CPF to the user in case of considering an active system, as presented in Section 2.

Finally, GNSS-SDR has evolved to integrate the core RTKLIB libraries for Single Point Positioning and Precise Point Positioning. The possibility to add the RTKLIB routines for applying WARTK DSM messages applicability would be feasible as a future add-on..

6 References

[1] Blewitt, G. (1990). An automatic editing algorithm for GPS data. Geophysical research letters, 17(3), 199-202

[2] Hernández-Pajares, M., Roma-Dollase, D., Krankowski, A., García-Rigo, A., & Orús-Pérez, R. (2017). Methodology and consistency of slant and vertical assessments for ionospheric electron content models. Journal of Geodesy, 91(12), 1405-1414.

[3] Hernández-Pajares, M., Juan, J. M., Sanz, J., & Colombo, O. L. (2000). Application of ionospheric tomography to real-time GPS carrier-phase ambiguities resolution, at scales of 400–1000 km and with high geomagnetic activity. Geophysical Research Letters, 27(13), 2009-2012.

[4] Hernández-Pajares, M., Juan, J. M., Sanz, J., & Aragón-Àngel, A. (2012). Propagation of medium scale traveling ionospheric disturbances at different latitudes and solar cycle conditions. Radio Science, 47(6).

[5] Hernández-Pajares, M., Wielgosz, P., Paziewski, J., Krypiak-Gregorczyk, A., Krukowska, M., Stepniak, K., ... & Orus-Perez, R. (2017). Direct MSTID mitigation in precise GPS processing. Radio Science, 52(3), 321-337.

[6] Hernández-Pajares, M., Roma-Dollase, D., Garcia-Rigo, A. (2017b). Examples of IGS real-time Ionospheric information benefits: Space Weather monitoring, precise farming and RT-GIMs. Oral presentation at IGS Workshop 2017, Paris, France.

[7] Roma-Dollase, D., Hernández-Pajares, M., Krankowski, A., Kotulak, K., Ghoddousi-Fard, R., Yuan, Y., ... & Feltens, J. (2017). Consistency of seven different GNSS globl ionospheric mpping techniques during one solr cycle. Journal of Geodesy, 1-16.

[8] Yang, H., Monte-Moreno, E., & Hernández-Pajares, M. (2017). Multi-TID detection and characterization in a dense Global Navigation Satellite System receiver network. Journal of Geophysical Research: Space Physics, 122(9), 9554-9575.

[9] Hadas, T., Krypiak-Gregorczyk, A., Hernández-Pajares, M., Kaplon, J., Paziewski, J., Wielgosz, P., …, Orus-Perez, R. (2017). Impact and implementation of higher-order ionospheric effects on precise GNSS applications. Journal of Geophysical Research: Solid Earth, 122. https://doi.org/10.1002/2017JB014750

7 Appendix

7.1 Post-fit residuals for the roving user AUT1 and the reference receiver SOFI

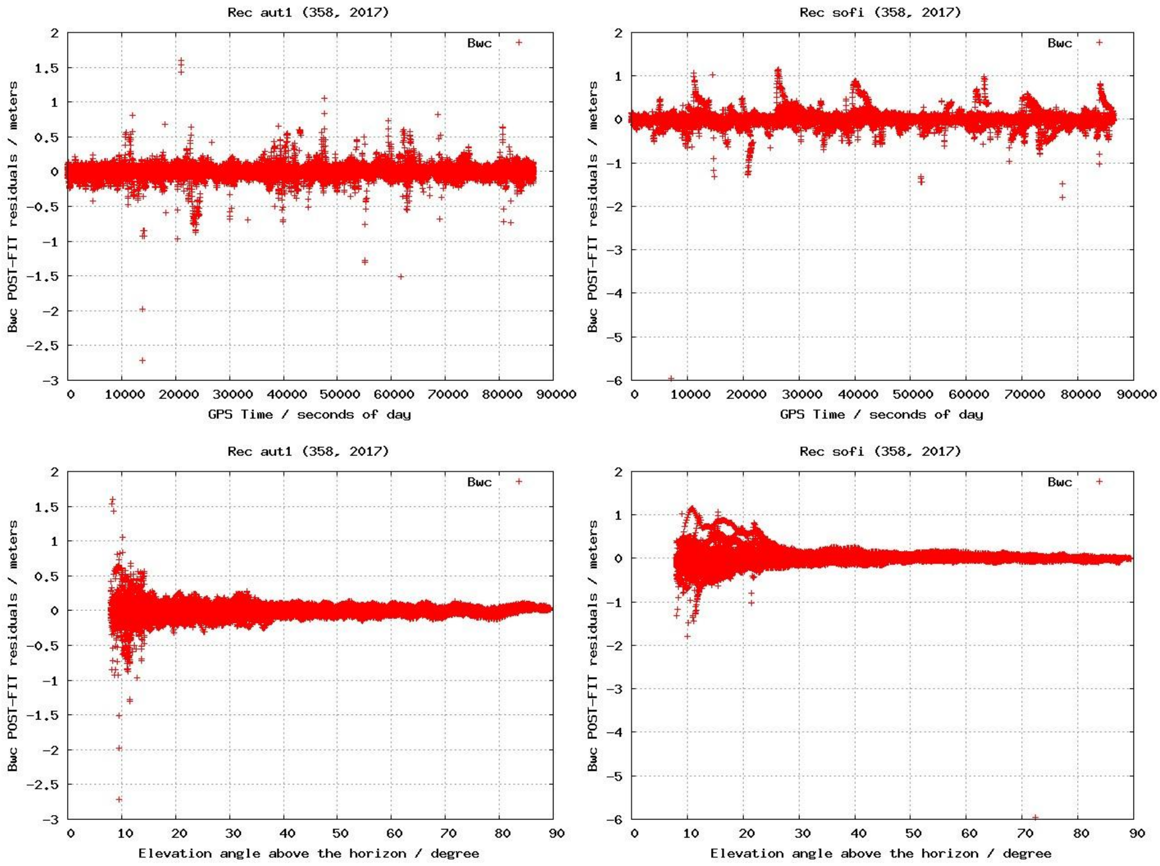

Figure 7.1 Post-fit residual for the Melbourne-Wübbena combination corresponding to the roving receiver AUT1 (first column) and the reference receiver SOFI (second column), versus time (first row) and versus elevation (second row), during day 25 December 2017.

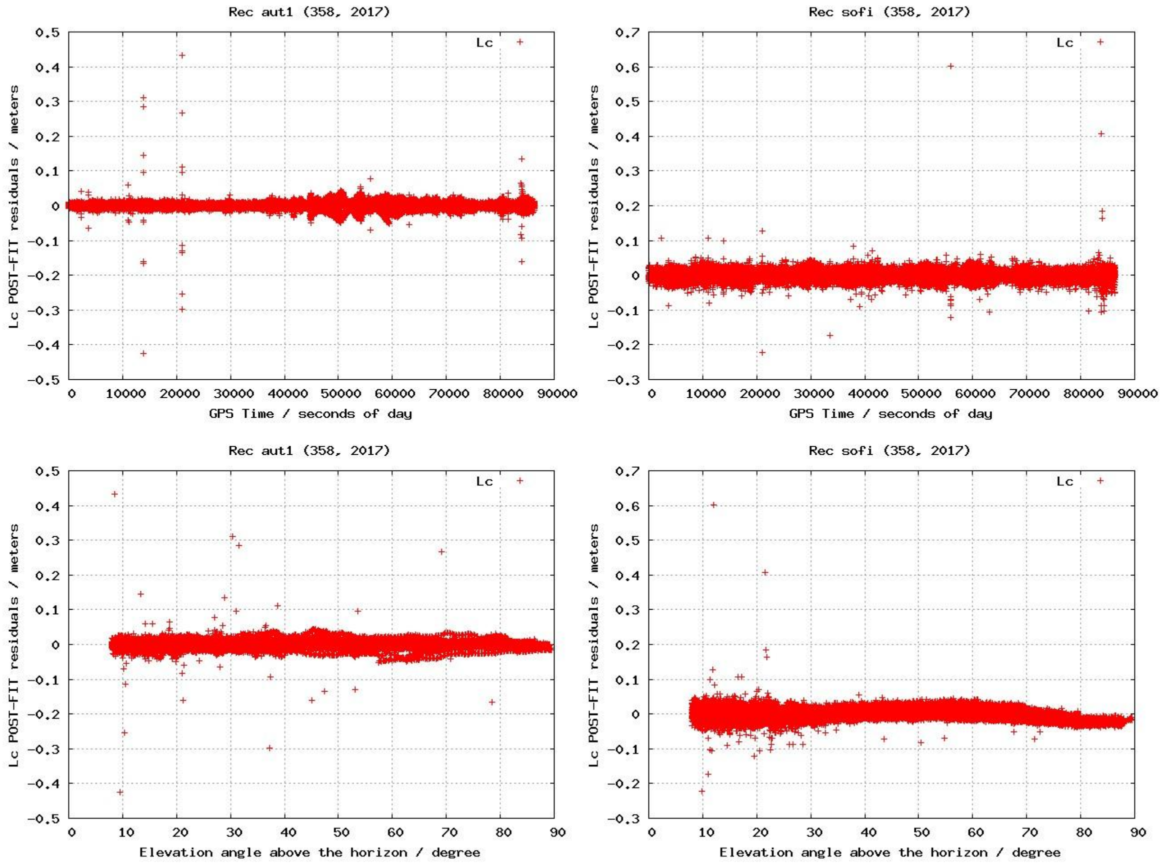

Figure 7.2 Post-fit residual for the ionospheric-free combination of the carrier phases corresponding to the roving receiver AUT1 (first column) and the reference receiver SOFI (second column), versus time (first row) and versus elevation (second row), during day 25 December 2017.

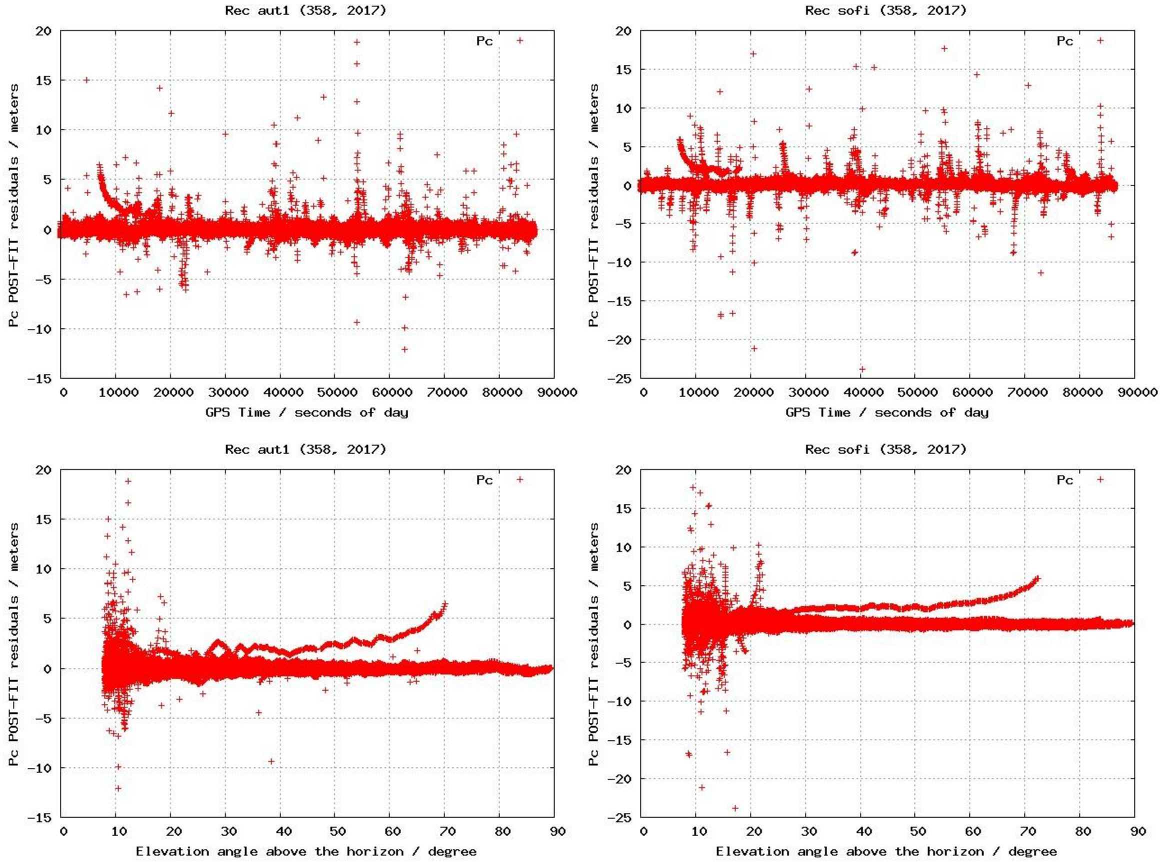

Figure 7.3 Post-fit residual for the ionospheric-free combination of the pseudoranges corresponding to the roving receiver AUT1 (first column) and the reference receiver SOFI (second column), versus time (first row) and versus elevation (second row), during day 25 December 2017.

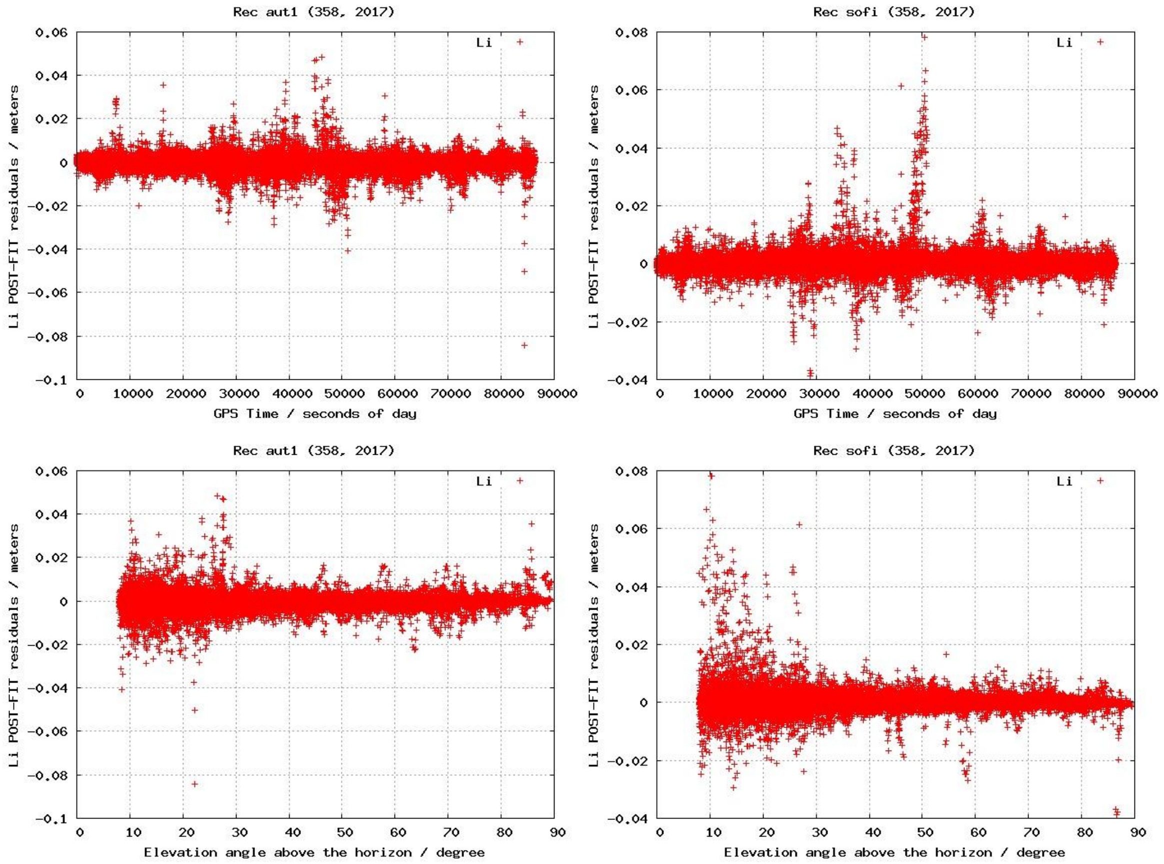

Figure 7.4 Post-fit residual for the ionospheric combination of the carrier phases corresponding to the roving receiver AUT1 (first column) and the reference receiver SOFI (second column), versus time (first row) and versus elevation (second row), during day 25 December 2017.